A&A 511, A32 (2010)
DOI: 10.1051/0004-6361/200912714

Astronomy & Astrophysics

The 15–20 μm PAH emission features: probes of individual PAHs?

C. Boersma[1], C. W. Bauschlicher Jr.[2], L. J. Allamandola[3], A. Ricca[2], E. Peeters[4,5], and A. G. G. M. Tielens[1,3]

[1] Kapteyn Astronomical Institute, University of Groningen, PO Box 800, 9700 AV, Groningen, The Netherlands
e-mail: C.Boersma@astro.rug.nl
[2] NASA Ames Research Center, MS 230-3, Moffett Field, CA 94035, USA
[3] NASA Ames Research Center, MS 245-6, Moffett Field, CA 94035, USA
[4] Department of Physics and Astronomy, PAB 213, The University of Western Ontario, London, ON N6A 3K7, Canada
[5] SETI Institute, 515 N. Whisman Road, Mountain View, CA 94043, USA

Received 17 June 2009 / Accepted 8 December 2009

ABSTRACT

Context. Spectral features between about 15−20 μm are commonly associated with polycyclic aromatic hydrocarbons (PAHs). With the NASA Spitzer Space Telescope these features are reported routinely, and as such, warrant a deeper molecular explanation.
Aims. We aim to determine the characteristics of the group of carriers of the plateau and the distinct sub-features at 15.8, 16.4, 17.4, 17.8 and 18.9 μm and to draw astronomical implications from these spectra.
Methods. We analyse and interpret the spectra of 15 different sources using the NASA Ames PAH IR spectroscopic database.
Results. The bands within the 15−20 μm region show large variations. Except for the 16.4 μm band, there is also no connection, both in band strength and feature classification, with the mid-IR PAH bands. Of the PAH spectra considered, only those from species containing pendent rings show one "common" characteristic: a band near the astronomical 16.4 μm position. However, coupling with the carbon skeleton's core influences its precise position in the spectrum. Compact PAHs in the size range 50−130 carbon atoms, consistently show a strong band near the astronomical 17.4 μm band position.
Conclusions. The 15−20 μm region is the transition zone from PAH nearest neighbour modes to full-skeleton modes. We conclude that a few individual PAHs dominate the astronomical PAH family when clear features are prominent. In the few cases of a broad plateau, the PAH family would be far richer. Although PAHs containing pendent rings showed promise explaining the astronomical 16.4 μm band, coupling with the skeleton core and the inherent strong quartet mode expected around 13.5 μm, make it a less viable candidate. The number of large PAHs in the database becomes a limitation in studying the emission between 15−20 μm and longward. Computation of larger PAH spectra should therefore be stimulated, especially for understanding the forthcoming far-IR data expected from Herschel, SOFIA and ALMA.

Key words. astrochemistry – molecular data – techniques: spectroscopic – infrared: general

1. Introduction

A group of emission features falling between 15 and 20 μm is observed in many objects that also show the well-known mid-IR PAH bands. This emission region is comprised of distinct narrow features and a broad variable plateau, with the most prominent features falling at 16.4 and 17.4 μm and a weak band at 15.8 μm (Boulanger et al. 1998; Moutou et al. 1998; Tielens et al. 1999; Moutou et al. 2000; van Kerckhoven et al. 2000). A broad emission plateau was identified by van Kerckhoven et al. (2000), spanning from 15 to 20 μm in the ISO-SWS spectra of a large variety of astronomical objects. With the arrival of the NASA Spitzer Space Telescope (Werner et al. 2004a) and its unprecedented sensitivity, these and other new sub-features are now reported routinely and can be studied systematically. Peeters et al. (2004) make a comparison between the early Spitzer data and ISO-SWS spectra and are able to infer that the sources that show a clear 17.4 μm feature also possess a relatively strong 16.4 μm feature. The classes as defined by Peeters et al. (2002) and van Diedenhoven et al. (2004) – on the basis of the spectral variations in the 3−15 μm region – do not appear to correlate strongly with the variations in the emission between 15−20 μm. This is consistent with the idea that larger PAHs than those responsible for the emission between 3−12 μm dominate the emission. Lastly, these authors are able to tie the discrete emission features to free floating PAH molecules by interpretation of their relatively narrow *FWHM* (~8 cm^{-1}).

Sellgren et al. (2007) re-visit NGC 7023 using Spitzer, obtaining spectra with the Infrared Spectrograph (Spitzer/IRS; Houck et al. 2004). Combining these with earlier high resolution spectra (Werner et al. 2004b) they confirm the detection of the individual bands at 16.4, 17.4 and 17.8 μm and report two weaker bands, at 15.8 and 18.9 μm. The long slit spectra show a variation in the strength of the plateau and individual features as a function of distance from the illuminating star. Their speculation on the carrier(s) of the 18.9 μm feature, which shows a $d^{-1.5}$ dependence, rules out minerals commonly associated with the ISM, "simple" PAHs, the carrier(s) of the extended red emission, and (nano)diamond(oid)s. From the Spitzer SINGS legacy program (Kennicutt et al. 2003), Smith et al. (2007b) report that all galaxies possess a strong PAH complex at "17" μm (not to be mistaken with the narrow 17.0 μm H_2 $S(1)$ rotational transition line), with only modest sub-features at 16.4 and 17.4 μm. The strength of the "17" μm complex correlates well with the strength of the 11.2 μm feature, suggesting a PAH origin. The luminosity of the "17" μm complex over 11.2 μm band also correlates well with the oxygen abundance. One interpretation is that, since longer wavelength features tend to arise from larger PAHs, PAH growth is stimulated by higher metallicities.

Table 1. Astrometric data.

Object	α [h m s] (2000)	δ [° ′ ″] (2000)	Distance [pc]	Ref.	Type of object
NGC 7023	21 01 36.9	+68 09 49	430	1	reflection nebula
NGC 2023	05 41 37.9	–02 15 52	470	2	reflection nebula
NGC 4736	12 50 53.2	+41 07 14	5.0×10^6	3	LINER galaxy
HD 36917	05 34 46.9	–05 34 15	510	4	Herbig Ae/Be star
HD 37411	05 38 14.5	–05 25 13	510	4	Herbig Ae/Be star
CN1-5	18 29 11.6	–31 29 59	46×10^2	5	planetary nebula
NGC 6567	18 13 45.1	–19 04 34	24×10^2	6	planetary nebula
LMC SMP036	05 10 39.7	–68 36 04	51×10^3	7	planetary nebula
LMC SMP038	05 11 23.8	–70 01 57	51×10^3	7	planetary nebula
LMC SMP061	05 24 36.0	–73 40 39	51×10^3	7	planetary nebula
IRAS 12063-6259	12 09 01.2	–63 15 56	95×10^2	8	HII region
Orion Bar Pos 1	05 35 18.3	–05 24 42	430	1	HII region
Orion Bar Pos 2	05 35 12.1	–05 26 09	430	1	HII region

References. (1) van den Ancker et al. (1997); (2) Perryman et al. (1997); (3) Smith et al. (2007b); (4) de Zeeuw et al. (1999); (5) Stanghellini & Pasquali (1995); (6) Cahn et al. (1992); (7) Kovács (2000); (8) Caswell & Haynes (1987).

Laboratory work and quantum-chemical calculations pave the way for identifying the carriers of 15−20 μm emission features and understanding the governing astrophysical conditions (experimental: Mattioda et al. 2009, and references therein; theoretical: Bauschlicher et al. 2009; Mulas et al. 2006 and references therein). The 15−20 μm wavelength region – characteristic for C−C−C bending modes – has received in the past much less attention than the shorter wavelength C−C and C−H stretching and bending modes in laboratory and computational studies. In preparation for the ISO mission (Kessler et al. 1996), Moutou et al. (1996) measured the absorption spectra of 40 neutral, salt matrix isolated, PAH molecules at wavelengths beyond 14 μm. That study predicted bands at 16.2, 18.2, 21.2 and 23.1 μm with strengths, in terms of that of the 6.2 μm feature, ranging from 13 to 70 percent. Later, combining the laboratory spectra from Schmidt et al. (unpublished) and Hudgins & Sandford (1998a,b,c), Moutou et al. (1998) have 22 percent of the data showing bands in the appropriate wavelength region. Within this extended data set, the large compact PAHs ($N_C \sim 32$) and those containing 5-membered rings show the strongest activity.

Using data from PAHs in the gas phase (Zhang et al. 1996), van Kerckhoven et al. (2000) concluded that the effect of ionisation on the bands between 15−20 μm are only moderate and that the distinct 16.4 μm feature arises from those PAHs in the sample that contain 5-membered rings. However, they note that the pentagons themselves are not producing the feature, but rather, the structures include pendent *hex*agonal rings in which a, so-called, "breathing-mode" causes the emission.

Recently, the NASA Ames PAH IR spectroscopic database has become available, containing over 580 calculated spectra. This unique database allows for the first time a consistent and systematic investigation of the characteristics of PAHs in the 15−20 μm wavelength region. The goal of this study is to use this database to characterise the carriers of the emitting features in the 15−20 μm wavelength range. Ricca et al. (2010) have looked at a set of large species, (C_{82}–C_{130}) not included in the version of the database used here (version 1.0). They have focussed on the far-IR ($\lambda \gtrsim 20$), the character of the individual modes and also touch upon the 15−20 μm region. This paper is organised as follows; in Sect. 2 the astronomical data are introduced (Sect. 2.1), analysed (Sect. 2.2) and the results are presented (Sect. 2.3). Section 3 introduces the NASA Ames PAH IR spectroscopic database and describes the methodology for using the synthetic data (Sect. 3.1). This is continued by analysing the spectra of different distinct groups of PAHs (Sect. 3.2) and ends by doing a "blind" search through the database for those PAH species that have their dominant emission band between 15−20 μm at 16.4 and 17.4 μm, respectively (Sect. 3.3). In Sect. 4, the results from both the astrophysical and theoretical study are combined and astronomical implications are drawn. A summary with conclusions is given in Sect. 5.

2. Observations

2.1. Astronomical spectra from 15–20 μm

Here, the 15 to 20 μm PAH emission features observed with NASA's Spitzer Space Telescope are presented. The chosen objects sample different astronomical environments, spanning the range of spectral variations observed in the 5–9 and 15−20 μm regions. This allows for a better understanding of the connections between local conditions and object type on one hand, and the spectral features and classification schemes on the other. Our sample consists of two Herbig Ae/Be stars; five planetary nebulae; three HII regions; two reflection nebulae, one with spectra at several positions; and spectra of SINGS galaxies. The utilised SINGS data consists of spectra at multiple positions in a single galaxy and the average spectrum from Smith et al. (2007b). The astrometric data on these sources are listed in Table 1.

Reflection nebulae: NGC 7023 is the reflection nebula in Cepheus irradiated by the Herbig Be star HD 200775. NGC 7023 has been thoroughly studied, most recently in the 15−20 μm PAH band region. The low-resolution 5 to 20 μm spectrum from Werner et al. (2004b), position A, is the representative for this type of object and its spectrum is presented in the top panel of Fig. 1. Several positions from Sellgren et al. (2007) have been selected to illustrate the spectroscopic variations across NGC 7023 (positions 1, 3 and 6 from slit C; 36, 19 and 48″ from HD 200775, respectively). NGC 2023 is the reflection nebula in Orion irradiated by the B star HD 37903. These data have been obtained from Peeters et al. (in prep.).

Galaxies: the galaxy spectra are taken from Smith et al. (2007b) and are part of the SINGS sample (Kennicutt et al. 2003). We obtained the average spectrum from Smith et al. (2007b) and use it as our representative spectrum for this type

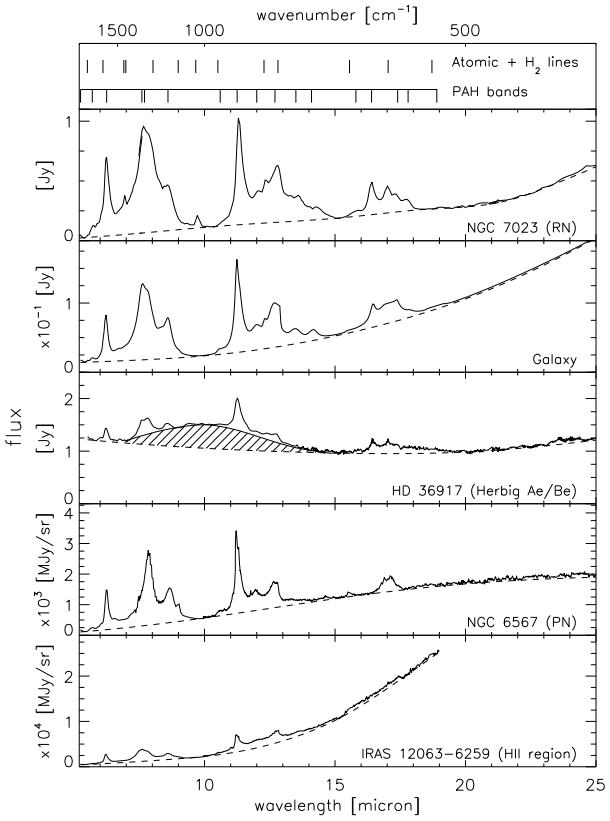

Fig. 1. The representative low-resolution 5.2−25 μm Spitzer IRS spectra for each of the five types of object studied here. The established continua are shown as the dashed lines. The hashed area in the spectrum of HD 36917 indicates the possible contribution due to silicates. The positions of the PAH bands, strong atomic and molecular hydrogen emission lines, which are listed in Table 2, have been indicated in the top frame.

of object. The low-resolution 5 to 20 μm average spectrum is presented in Fig. 1. Enhanced data products have been obtained from the SSC, and from that collection NGC 4735 has been chosen to illustrate the variations in the 15−20 μm region across a single galaxy.

***Herbig Ae/Be stars*:** HD 36917 is a non-isolated Herbig Ae/Be star located South of the Orion belt in the OB1c association and has been identified as a spectroscopic binary (Levato & Abt 1976). HD 37411 is also located in Orion's belt OB1c association. These data are part of the Spitzer program with PID 3470. Both spectra have been studied earlier by Boersma et al. (2008), where the profile variations of the "7.7" μm feature were investigated. The spectrum of HD 36917 is our representative spectrum for this type of object and it is presented in Fig. 1. Note that both sources have strong emission from silicates contributing to their spectrum.

***Planetary nebulae*:** NGC 6567 and CN1-5 are two Galactic planetary nebulae located in Sagittarius. For both sources, the BCD data have been retrieved from the SSC and reduced using CUBISM (Smith et al. 2007a). For NGC 6567, a background obtained from a designated sky observation was subtracted. Bad pixels were removed by using the default values for global and record bad pixel cleaning within CUBISM. The extraction aperture was taken to include the source in the Short-Low (SL) observations (10 and 8 pixels for NGC 6567 and CN1-5, respectively). However, this aperture falls partly outside the SH/LH FOV. Therefore, we applied a slightly different aperture for the SH/LH data in order to restrict it within the FOV (8 and 4 pixels for the SH and LH modules, respectively). To check for aperture effects, we extracted spectra for both the SL apertures and the adapted SH/LH aperture and found little difference. NGC 6567 is our representative for this type of object and its low-resolution 5−20 μm spectrum is presented in Fig. 1. The planetary nebulae LMC SMP036, LMC SMP038 and LMC SMP061 are located in the Large Magellanic Cloud. As part of a larger group, these planetary nebulae have been studied by Bernard-Salas et al. (2009). We have obtained the data from these authors.

Table 2. Atomic and molecular hydrogen emission features found in the spectra shown in Fig. 1.

Feature	Wavelength [μm]
H_2S(7)	5.511
H_2S(6)	6.109
H_2S(5)	6.909
H_2S(4)	8.026
H_2S(3)	9.665
H_2S(2)	12.278
H_2S(1)	17.035
H_2S(0)	28.221
[ArII]	6.985
[ArIII]	8.991
[SIV]	10.511
[NeII]	12.813
[NeIII]	15.555
[SIII]	18.713

***HII regions*:** the Orion Bar is the photon dominated region that forms the interface between the bright HII region that is ionised by the Trapezium stars and the Orion Molecular Cloud. The spectra presented here are of two positions in the bar; one close to the ionising stars and the other further away. The data on both positions have been obtained from Peeters et al. (2006). IRAS 12063-6259 is a roughly triangular nebular compact HII region. Spectroscopic data on this source was obtained from Otaguro et al. (in prep.). The low-resolution 5−20 μm spectrum of IRAS 12063-6259, shown in Fig. 1, is our representative for this type of object. Note that no Spitzer data beyond 20 μm are available for this source.

For detailed descriptions on the initial reduction of the data presented here, we refer to the references provided above. Additional reduction on the data included splicing of the different orders and modules and masking strong emission lines and bad data. When available, the high-resolution spectrum has been used in our analysis.

2.2. Decomposition of the astronomical spectra

To facilitate comparison between the astronomical data and the PAH spectra in the database, continua have been constructed and subtracted from the astronomical spectra. Several approaches for establishing these continua exist (e.g., Smith et al. 2007b; Sellgren et al. 2007). We adopt those from Peeters et al. (2002); van Diedenhoven et al. (2004); Hony et al. (2001) and van Kerckhoven et al. (2000). The different emission components are established in the following manner: a global

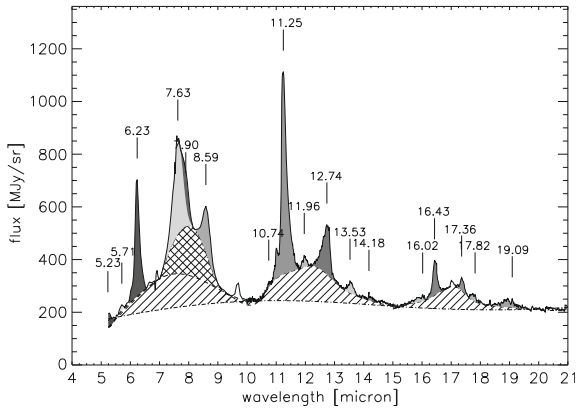

Fig. 2. The combined high and low-resolution 5.2–21 μm Spitzer-IRS spectrum for the Reflection Nebula NGC 2023 illustrating the continuum, band and plateau identification as described in Sect. 2.2. The bands are shaded grey and their peak positions have been indicated (in μm) above the band. The hashed regions show the plateaus and the double hashed region is the 7–10 μm "sub"-plateau.

spline continuum is drawn connecting points near 5.5, 10, 15 and 20 μm. The individual PAH bands are isolated by bracketing the features using local splines in four distinctive wavelength regions; 5–6, 7–10, 10–15 and 15–20 μm. A spline connecting points near 5.5, 7 and 10 micron is first determined for the 7–10 μm region. The "7.7" and 8.6 μm features are then further isolated by drawing a spline connecting points near 7, 8.3 and 9 μm. Finally, the blended 7.6 and 7.8 μm bands are decoupled using a 'blind' Gaussian fit, where the peak positions and widths of both components are allowed to vary marginally. Overall, the decompositions are of good quality. The plateaus naturally arise as the differences between the local splines and the global spline continua. The result from this analysis on the spectrum of NGC 2023 is shown in Fig. 2.

In contrast, Sellgren et al. (2007) use multiple Gaussians to decompose the 15–20 μm region into distinct components, with a broad emission component at 17.2 μm underlying the overall emission. Smith et al. (2007b) use a similar approach but find the broad component centred at 17.0 μm. We have treated the broad underlying component as part of the 15–20 μm plateau. Detailed comparison between these two methods have demonstrated that there are systematic differences in the derived strengths of the various emission features, but that general trends are independent of the method employed (Galliano et al. 2008).

Besides the strong PAH features at 6.2, "7.7", 11.2 and 12.7 μm, most sources show after continuum subtraction also bands at 5.25, 5.7, 10.6, 12.0, 13.5, 14.1 μm and weak satellite features at 6.0 and 11.0 μm. Figure 3 presents the global continuum subtracted 15–20 μm spectral region for all the sources and positions within sources studied here. The region generally consists of a broad component, often underlying much narrower features of variable intensity at 15.8, 16.4, 17.4, 17.8 and 18.9 μm. The peak positions of the emission features between 5–20 μm for all of the objects considered are listed in Table 3. The peak position is the resolution element at which the band reaches maximum intensity. Table 3 also gives the PAH profile classes as described in Peeters et al. (2002) and van Diedenhoven et al. (2004). For the 6.2 and 11.2 μm features the classes are assigned based on their peak position. For the "7.7" μm band the 7.8/7.6 μm integrated band strength ratio is used as class indicator.

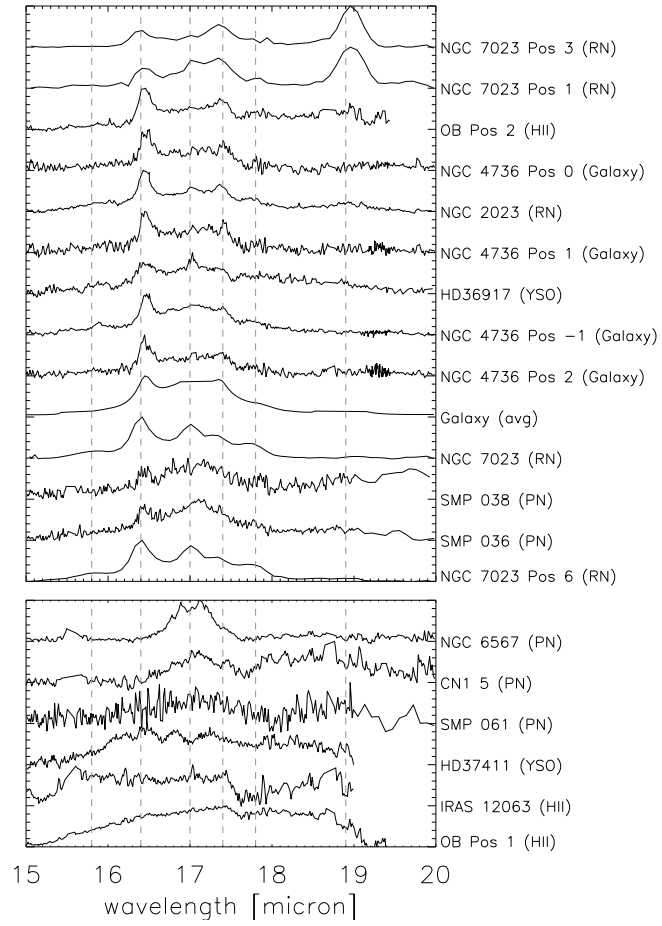

Fig. 3. A comparison of the 15–20 μm spectra for all objects and positions within objects considered (OB = Orion Bar). All spectra have been continuum subtracted and their strongest peak normalised to unity. The dashed vertical lines show the positions of the 15.8, 16.4. "17.0", 17.4, 17.8, and 18.9 μm bands. The spectra have been sorted according their 16.4/17.4 μm band strength ratio. The five spectra in the *bottom panel* have been set apart because of their substantially different nature.

Perusal of the spectra shown in Fig. 3 and the peak positions listed in Table 3, shows that there is much greater variation in the 15–20 μm PAH features than there are in the more familiar 5–15 μm PAH features. These variations between 15–20 μm are not only evident between different object types, but also within extended objects. To quantitatively assess these variations, the strengths of these bands have been determined. Note that the wavelength range for the 5.25 μm PAH band is not completely covered by Spitzer. Therefore, its properties are determined by fitting a Gaussian to the available (>5.2 μm) data. Finally, although no "true" continuum might have been established, its determination is consistent over the sample and any deviation from it should be systematic. An estimated accuracy of 10–20% is determined from several rounds of drawing continua and calculating band strengths.

Amorphous and crystalline silicate emission can blend with the PAH features between 7–20 μm. This is clearly the case for the two Herbig Ae/Be stars HD 36917 and HD 37411. An indication of the silicate contribution to the spectrum of HD 36917 between 5–15 μm is shown as the dashed area in Fig. 1. Weaker silicate emission is also expected around 18 and 23 μm. It should be noted that even when no evidence for silicate emission is present between 5–10 μm, it might still be present at longer wavelengths ($\gtrsim$15 μm), e.g., HD 44179 ("Red Rectangle"; Waters et al. 1998).

Table 3. Peak positions and ABC band classifications for the PAH emission features between 5–20 μm.

Source	PAH band [μm]														
	5.25 [μm]	5.7 [μm]	6.2 [μm]	7.6 [μm]	7.8 [μm]	8.6 [μm]	10.6 [μm]	11.2 [μm]	12.0 [μm]	12.7 [μm]	13.5 [μm]	14.1 [μm]	15.8 [μm]	16.4 [μm]	17.4 [μm]	17.8 [μm]	18.9 [μm]
NGC 7023	5.23	5.73	6.25/B	7.62/A	7.90/A	8.63	10.81?	11.30/B	12.02	12.81	13.59	14.32	15.82	16.42	17.35	17.77	19.04
NGC 7023 Pos 1	–	–	–	–	–	–	–	–	–	–	–	?	15.82	16.42	17.35	17.86	18.96
NGC 7023 Pos 3	–	–	–	–	–	–	–	–	–	–	–	?	15.57?	16.42	17.35	17.94	18.96
NGC 7023 Pos 6	–	–	–	–	–	–	–	–	–	–	–	?	15.82	16.42	17.35	17.86	19.04
NGC 2023	5.23	5.71	6.23/A	7.63/A	7.90/A	8.59	10.74	11.25/A	11.96	12.74	13.53	14.18	16.02	16.43	17.36	17.82	19.09
Galaxy (avg)	5.26	5.72	6.23/A	7.62/A	7.90/A	8.62	10.53	11.24/A	11.98	12.69	13.47	14.18	15.86?	16.45	17.39	17.86	19.15
NGC 4736 Pos 2	–	–	–	–	–	–	10.54	11.21/A	11.96	12.73	13.62	14.17	15.82	16.45	17.40	17.90	19.16?
NGC 4736 Pos 1	–	–	–	–	–	–	10.53	11.23/A	12.00	12.73	13.62	13.99	16.02	16.45	17.40	17.91	18.62?
NGC 4736 Pos 0	–	–	–	–	–	–	10.54	11.22/A	11.96	12.72	13.62	14.18	16.09?	16.50	17.40	17.81?	18.88?
NGC 4736 Pos -1	–	–	–	–	–	–	10.60	11.27/B	12.00	12.81	13.55	14.26	15.89	16.47	17.40	17.69	19.28?
HD 36917		5.70	6.22/A	7.68/AB	7.86/AB	8.54	10.60	11.27/B	12.05	12.78	13.78	14.13	15.88	16.39	17.40	17.85?	18.85?
HD 37411	–	5.73	6.25/B	7.56/B	7.80/B	8.66	10.06	11.27/B	11.93	12.66	13.26	14.18	16.22?	16.48?	17.24?	17.94?	18.31?
CN1 5	5.29	5.74	6.27/B	7.50/B	7.90/B	8.71	10.57	11.25/B	12.00	12.71	13.42	14.35?	16.07?	16.50?	17.47	17.88	19.06?
NGC 6567	5.26	5.68	6.23/A	7.53/B	7.85/B	8.71	10.56	11.21/A	11.95	12.80	13.33	14.63	16.01?	16.50?	17.11?	17.45?	19.05?
LMC SMP036	5.40?	5.64	6.24/B	7.40/B	7.87/B	8.72	10.61?	11.23/A	11.83	12.82	13.41	14.22	15.95?	16.45	17.53?	17.78	18.79?
LMC SMP038	5.24	5.60	6.22/A	7.63/B	7.85/B	8.65	10.73?	11.18/A	11.99	12.73	13.76	14.55	16.00?	16.41	17.57?	17.86	18.67?
LMC SMP061	3.50?	5.64	6.24/B	7.56/B	7.81/B	8.66	10.50?	11.21/A	11.70	12.62	13.29	13.95?	16.10?	16.63?	17.36?	17.87?	18.67?
IRAS 12063-6259	5.19	5.71	6.20/A	7.58/A	7.87/B	8.59	10.54	11.21/A	11.98	12.84	13.54	14.02?	15.85?	16.47?	17.44	17.69?	18.63?
Orion Bar Pos 1	–	–	–	–	–	–	10.72	11.20/A	12.00	12.79	13.55	14.00?	15.90?	16.50?	17.44	17.89?	19.08?
Orion Bar Pos 2	–	–	–	–	–	–	10.58	11.22/A	12.00	12.79	13.53	14.22	16.23?	16.41	17.36	17.89?	18.95?

Notes. 1) a "–" indicates there are no data available; 2) a "?" indicates an uncertain band identification; 3) the blended 7.6 and 7.8 bands have been separated using Gaussians.

Some indications for emission around 23 μm are present in the spectra of HD 36917 and NGC 7023. Silicate emission may also contribute weakly to the plateaus. A proper separation of both emission components would require a full mineralogical decomposition, an analysis which is beyond the scope of this study.

Strong atomic and hydrogen emission lines can also blend in with the PAH band features, especially at 12.8 μm ([NeII]), 15.6 ([NeIII]), 17.0 (H_2 S(1)) and 18.7 μm ([SIII]). The data points associated with the strongest lines have been masked in the spectra when integrating the PAH bands. However, the shoulders might not have been completely accounted for and weaker lines not removed. This might influence the measured band strengths, determined peak positions (e.g., of the 12.7 μm PAH band) and the plateau strengths (e.g., between 15–20 μm). Even so, the relative contributions are minor, leading to uncertainties of typically a few percent.

The quality of the 5–10 μm spectra is good for all sources considered and we estimate an uncertainty of less than 10% for the integrated band strengths in this region. In contrast, the quality of the 10–15 μm data is variable in the different spectra. For the best quality spectra, we again estimate an uncertainty of less than 10%. For the lower quality data, we estimate an uncertainty of 20%. The quality of the data between 15–20 μm is generally low and we estimate an uncertainty of 20% for the best data and of 40% for the worst. Table 4 presents the strengths for the identified PAH bands. The strengths of the underlying plateaus are presented in Table 5.

2.3. The 15–20 μm features

Figure 3 compares the continuum subtracted and normalised 15–20 μm spectra of all the sources and positions within sources studied here. In this figure the spectra have been ordered according to their 16.4/17.4 μm integrated band strength ratio. From this figure, several similarities and differences become apparent.

The 16.4 μm feature is present in most spectra, as is the 17.4 μm feature. Underneath the 16.4 and 17.4 μm features lies the broad "17" μm plateau/feature, identifiable in almost all spectra and particularly distinguishable in NGC 6567. A very broad, almost structureless plateau is characteristic for the spectra of IRAS 12063-6259 and the first Orion Bar position – closest to the ionising stars –, although there is some indication for the presence of the 17.4 μm feature in both spectra. The 15.8 μm feature is only detected in ~50% of the spectra. A distinct emission feature around 17.8 μm is identifiable in 75% of the spectra, however, it is strikingly absent in IRAS 12063-6259. The 18.9 μm feature is dominant in the spectra of NGC 7023 positions 1 and 3. Other detections seem more tentative. What Fig. 3 furthermore shows, is that the 15–20 μm bands are not obviously related.

The intensities in the bands are analysed using ratios. Ratios are chosen in particular, because when comparing good quality spectra from faint objects to much brighter objects, the ratio approach narrows the dynamic range and allows one to focus on the small variations. In other words, the ratio approach is a type of normalisation that emphasises differences rather than absolute intensities.

However, not all sources provide reliable ratios. The presence of silicate emission in the spectrum of the two Herbig Ae/Be stars hampers the band strength measurements between 5–15 μm. Therefore, they have been omitted. Furthermore, the spectral shape for a few sources is dramatically different between 15–20 μm–the five sources set apart in Fig. 3 – and in a few other cases, not the entire 5–20 μm wavelength range is

available and certain ratios are not established. These sources have also been omitted.

In Fig. 4, two earlier established correlations are verified for this small and selective sample. Both the "7.7"/11.2 versus 6.2/11.2 μm band strength ratios and the relation between the "17" μm emission band and the 11.2 μm PAH band are present in our sample. The good correlation between the 6.2/11.2 vs. "7.7"/11.2 μm integrated band strength ratios is well established for a wide variety of sources (Hony et al. 2001; Peeters et al. 2002; Galliano et al. 2008) and is taken to trace the ionisation balance of interstellar PAHs. The "17" μm emission band is here defined as the sum of all emission between 15−20 μm and the good correlation confirms a PAH origin for the emission between 15−20 μm. Smith et al. (2007b) have shown for the considerably larger SINGS galaxy sample that the "17" μm complex correlates well with the 11.2 μm band.

The connection between the variations in the 15−20 (C−C−C) and the variations in the 11−15 (C−H) and those in the 6−9 μm (C−C) spectral regions have also been investigated. Figure 5 shows the best correlation; that of the 16.4 and the 6.2 μm band. No clear relationship could be identified for the other bands between 15−20 μm with any of the PAH bands (6.2, "7.7", 11.2 and 12.7 μm), although sometimes those were limited by the number of data points.

Peeters et al. (2004) have investigated the relation between the 15−20 μm bands and the mid-IR PAH band classification. Specifically, the "7.7" μm band was classified as A, B or C depending on the peak position of this band. A similar result was obtained for the 6.2 μm band. Here, we study the relationship of the 15−20 and "7.7" μm bands, using two different indicators. First, the wavelength at which half the intensity in the entire band has been reached (conform Sloan et al. 2005). Second, the 7.8/7.6 μm integrated band strength ratio. In this analysis, only the 16.4 μm band shows a correlation with the mid-IR band classification, which is clearest when using the 7.8/7.6 μm integrated band strength ratio as class indicator, Fig. 6.

In Fig. 7, three band strength ratios plots are presented. A weak correlation seems to be present for the 13.5/11.2 with the 16.4/11.2 μm integrated band strength ratios, but with clear outliers. A tentative trend also appears between the 16.4 μm over the total integrated band strength between 15−20 μm and the 12.7/11.2 μm integrated band strength ratio, although, the average spectrum of the galaxies is a clear outlier. Perhaps, this is not that surprising, considering this point represents the average taken over many different kinds of galaxies. Lastly, the the total integrated band strength between 15−20 μm over the total integrated PAH emission versus the 11.2 μm over the total integrated PAH emission band strength ratios shows a tentative trend.

In summary, two major narrow components – at 16.4 and 17.4 – are prominent in many sources. These two components are generally perched on a broad "17" μm band. In one case, the latter band fully takes over the spectral structure in this region (NGC 6567). In addition, we also recognise narrow bands at 15.8, 17.8 and 18.9 μm (Sellgren et al. 2007), which are clearly found in some spectra, but not in a majority of the spectra. A few spectra show only a broad component spanning the full wavelength range, which may well represent a blend of all narrow components, e.g., Orion Bar Position 1.

The observations also show that the individual emission components in the 15−20 μm region are not correlated with each other, nor do they correlate well with the mid-IR PAH emission features, either by band strength or profile class. An exception is the 16.4 μm feature, which does show tentative connections with the 6.2, 13.5 and feature classification of the "7.7" μm bands.

Table 4. Integrated band strengths for the PAH emission features between 5−20 μm.

Source	PAH band [μm]																	
	5.25	5.7	6.2	7.6	7.8	8.6	10.6	11.2	12.0	12.7	13.5	14.1	15.8	16.4	17.4	17.8	18.9
NGC 7023	8.25e-16	5.13e-16	8.64e-15	8.09e-15	5.39e-15	1.38e-15	6.85e-17	5.23e-15	1.20e-16	1.80e-15	2.45e-16	1.35e-17	7.46e-17	5.40e-16	4.35e-17	1.20e-16	5.05e-17
NGC 7023 Pos 1	–	–	–	–	–	–	–	–	–	–	–	?	9.07e-17	1.15e-16	6.19e-17	3.28e-17	3.55e-16
NGC 7023 Pos 3	–	–	–	–	–	–	–	–	–	–	–	?	9.88e-17	4.53e-16	5.29e-16	5.84e-17	1.27e-15
NGC 7023 Pos 6	–	–	–	–	–	–	–	–	–	–	–	?	3.94e-16	2.48e-15	1.27e-16	5.93e-16	3.68e-16
NGC 2023*	1.67e-12	2.79e-13	6.92e-12	7.40e-12	1.35e-12	2.22e-12	5.53e-14	4.69e-12	1.44e-13	1.14e-12	1.73e-13	7.16e-14	8.78e-14	2.76e-13	8.41e-14	5.42e-14	1.36e-13
Galaxy (avg)	1.06e-16	3.49e-17	8.47e-16	1.34e-15	3.38e-16	3.43e-16	2.55e-17	7.37e-16	1.81e-17	3.61e-16	3.57e-17	3.10e-17	3.52e-19	3.91e-17	6.86e-18	3.09e-18	2.37e-17
NGC 4736 Pos 2*	–	–	–	–	–	–	1.32e-14	1.33e-13	7.11e-15	3.98e-14	4.15e-15	3.89e-15	1.46e-16	6.72e-15	1.44e-15	1.87e-15	8.38e-16
NGC 4736 Pos 1*	–	–	–	–	–	–	6.57e-15	1.01e-13	7.42e-15	3.71e-14	5.16e-15	2.84e-15	1.18e-15	5.85e-15	1.46e-15	1.14e-15	1.29e-15
NGC 4736 Pos 0*	–	–	–	–	–	–	1.20e-14	1.02e-13	7.44e-15	3.67e-14	3.54e-15	2.86e-15	1.37e-15	5.11e-15	1.79e-15	1.09e-15	7.73e-16
NGC 4736 Pos -1*	–	–	–	–	–	–	3.05e-14	3.46e-13	2.33e-14	8.17e-14	4.98e-15	5.90e-15	3.36e-15	1.18e-14	2.69e-15	3.05e-15	1.69e-15
HD 36917	–	3.37e-16	2.67e-15	8.00e-15	3.31e-16	1.15e-15	1.92e-16	4.12e-15	1.44e-16	9.09e-16	1.88e-16	2.12e-16	1.60e-16	3.07e-16	7.31e-17	2.62e-16	9.91e-17
HD 37411	–	3.40e-16	2.47e-15	5.26e-16	3.07e-15	1.03e-15	2.01e-16	7.37e-16	6.97e-17	3.10e-16	9.45e-17	7.19e-17	7.23e-17	9.89e-17	1.15e-16	4.77e-17	1.37e-16
CN1 5*	1.20e-13	2.38e-13	3.53e-12	1.22e-12	5.78e-12	1.64e-12	3.63e-13	3.06e-12	1.08e-13	8.01e-13	3.30e-13	1.77e-13	7.87e-14	3.10e-14	8.00e-14	3.00e-13	2.95e-14
NGC 6567*	5.14e-13	1.44e-12	1.60e-11	3.41e-12	2.69e-11	9.87e-12	1.35e-12	1.24e-11	6.89e-13	3.53e-12	4.01e-13	6.64e-13	8.21e-14	8.61e-14	1.11e-13	9.75e-14	3.80e-13
LMC SMP036	3.19e-17	3.25e-16	2.03e-15	8.99e-16	2.06e-15	5.43e-16	2.67e-17	2.00e-15	1.01e-16	5.31e-16	4.79e-17	5.62e-17	7.16e-18	6.63e-17	3.51e-18	1.51e-17	4.19e-17
LMC SMP038	1.72e-16	9.47e-17	4.98e-16	4.18e-16	4.76e-16	1.67e-16	3.09e-18	6.65e-16	2.99e-17	1.23e-16	3.83e-17	8.40e-17	3.60e-18	1.40e-17	7.97e-19	9.45e-18	1.44e-17
LMC SMP061	4.69e-16	3.98e-17	3.75e-16	–	6.92e-16	1.75e-16	5.82e-17	4.70e-16	3.05e-17	1.24e-16	3.18e-17	2.14e-17	7.39e-18	1.09e-17	7.36e-19	?	2.54e-17
IRAS 12063-6259*	3.87e-12	1.73e-12	2.55e-11	4.46e-11	6.70e-12	1.03e-11	1.58e-12	1.53e-11	2.40e-13	8.20e-12	1.63e-12	1.57e-13	2.19e-13	2.87e-13	8.18e-13	3.95e-13	2.61e-12
Orion Bar Pos 1*	–	–	–	–	–	–	9.21e-13	4.26e-11	3.44e-12	2.10e-11	2.98e-12	2.05e-12	8.30e-13	3.50e-12	3.84e-12	3.12e-12	4.47e-12
Orion Bar Pos 2*	–	–	–	–	–	–	4.95e-13	2.11e-11	7.53e-13	7.22e-12	7.56e-13	4.22e-13	2.53e-14	1.26e-12	6.21e-13	4.07e-13	0.00e-00

Notes. 1) units are in W m^{-2} or MW m^{-2}/sr for the sources with a "*"; 2) a "–" indicates there are no data available.

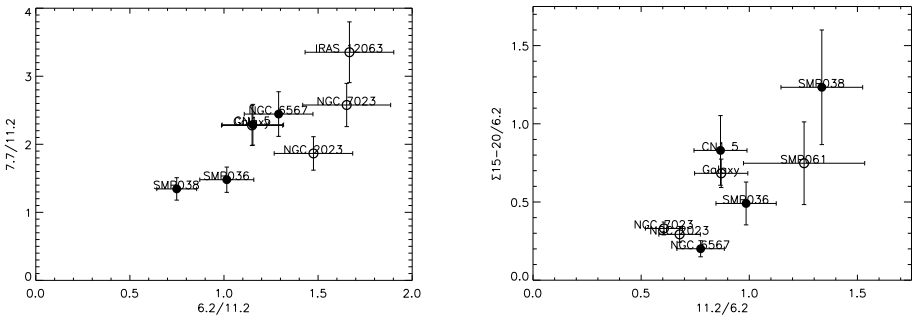

Fig. 4. Two earlier established PAH band correlations. Peeters et al. (2002) class A sources are shown as open circles and class B sources as filled circles.

Table 5. Integrated plateau strengths for the PAH plateaus between 5–20 μm.

Source	PAH plateau [μm]		
	5–10	10–15	15–20
NGC 7023	4.67e-14	1.37e-14	2.03e-15
NGC 7023 Pos 1	–	–	9.27e-16
NGC 7023 Pos 3	–	–	1.14e-15
NGC 7023 Pos 6	–	–	1.16e-14
NGC 2023	2.83e-11	6.84e-12	1.39e-12
Galaxy (avg)	4.63e-15	1.65e-15	5.06e-16
NGC 4736 Pos 2*	–	1.66e-13	3.41e-14
NGC 4736 Pos 1*	–	1.23e-13	1.84e-14
NGC 4736 Pos 0*	–	1.38e-13	2.26e-14
NGC 4736 Pos -1*	–	4.37e-13	1.04e-13
HD 36917 (+sil.)	3.57e-16	4.18e-14	2.73e-15
HD37411 (+sil.)	6.24e-15	8.16e-15	1.56e-15
CN1 5*	9.04e-12	8.73e-12	2.41e-12
NGC 6567*	6.46e-11	1.99e-11	2.46e-12
LMC SMP036	7.87e-15	2.34e-15	8.62e-16
LMC SMP038	2.88e-15	1.14e-15	5.72e-16
LMC SMP061	1.70e-15	1.15e-15	2.36e-16
IRAS 12063-6259*	1.06e-10	8.18e-11	1.71e-11
Orion Bar Pos 1*	–	1.13e-10	2.44e-10
Orion Bar Pos 2*	–	3.58e-11	8.23e-12

Notes. 1) units are in W m^{-2} or MW m^{-2}/sr for the sources with a "*"; 2) a "–" indicates there are no data available.

In addition, weak correlations exist between the 12.7/11.2 and 16.4/$\sum$15–20 μm integrated band strength ratios and the 11.2 and $\sum$15–20 μm PAH bands.

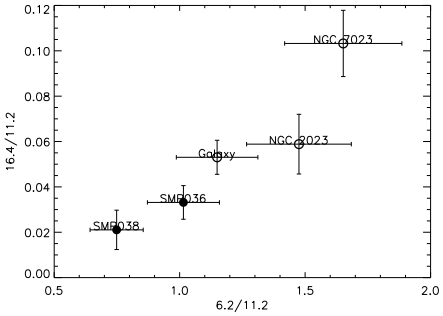

Fig. 5. The good correlation of the 16.4 with the 6.2 μm (C–C) mode. Peeters et al. (2002) class A sources are shown as open circles and class B sources as filled circles.

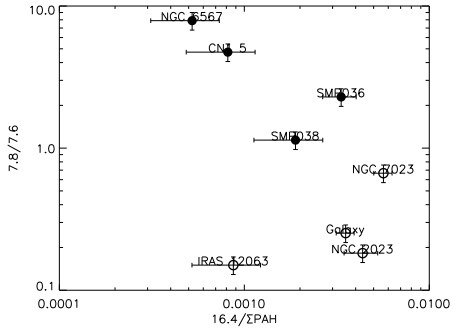

Fig. 6. Connection of the 16.4 μm feature with the ABC PAH classification of the "7.7" μm band (Peeters et al. 2002), using the 7.8/7.6 μm integrated band strength ratios as an A/B class indicator. Class A and B sources are shown as open and filled circles, respectively.

3. PAH spectroscopic properties from 15–20 μm

Here, we discuss the 15–20 μm region of the theoretically computed PAH spectra that have been assembled at NASA's Ames Research Center. Thus far, over 580 spectra have been computed. Together with a selection of 60 experimental measured spectra, they constitute the steadily growing NASA Ames PAH IR spectroscopic database (Bauschlicher et al., in prep.; Mattioda et al., in prep.). This database, with additional on-line tools, will be made publicly available beginning of 2010.

3.1. Synthetic PAH spectra

The NASA Ames PAH IR spectroscopic database contains spectra computed using density functional theory (DFT) making use of the hybrid (Becke 1993) B3LYP (Stephens et al. 1994) approach in conjunction with the 4-31G basis set (Frisch et al. 1984). Geometries are fully optimised and harmonic frequencies are computed using analytic second derivatives. All of the DFT calculations are performed using the Gaussian 03 program system (Frisch et al. 2004). This level of theory has been compared with mid-IR experimental spectra and, provided the computed harmonic frequencies are scaled by 0.958, the overall agreement is very good.

We (re-)investigate the choice of scaling factor for the 15–20 μm region by fitting computed spectra in this region to the experimentally obtained spectra of 13 molecules: pentacene ($C_{22}H_{14}$), coronene ($C_{24}H_{12}$), dibenzo-pyrene ($C_{24}H_{14}$), 3, 4; 5, 6; 7, 8-tribenzoperopyrene ($C_{34}H_{16}$), 3, 4; 5, 6; 7, 8; 12, 13-tetrabenzoperopyrene ($C_{36}H_{16}$), 3, 4; 5, 6; 10, 11; 12, 13-tetrabenzoperopyrene ($C_{36}H_{16}$), dibenzoheptacene ($C_{36}H_{20}$), dianthraceno-pyrene ($C_{40}H_{22}$), 1,14-benzodiphenanthreno-(1′′′′, 9′′′′;2, 4), (9′′′′, 1′′′′; 11, 13)-bisanthene ($C_{50}H_{22}$), 12, 13-o-phenylene-1, 2; 3, 4; 5, 6; 7, 8; 9, 10-pentabenzoperopyrene ($C_{48}H_{22}$), 12, 13-o-phenylene-3, 4; 5, 6; 7, 8-tribenzoterrylene ($C_{40}H_{18}$), difluoranthen-(3′, 5′; 4, 6),(4′′′, 6′′′; 9, 11)-coronene

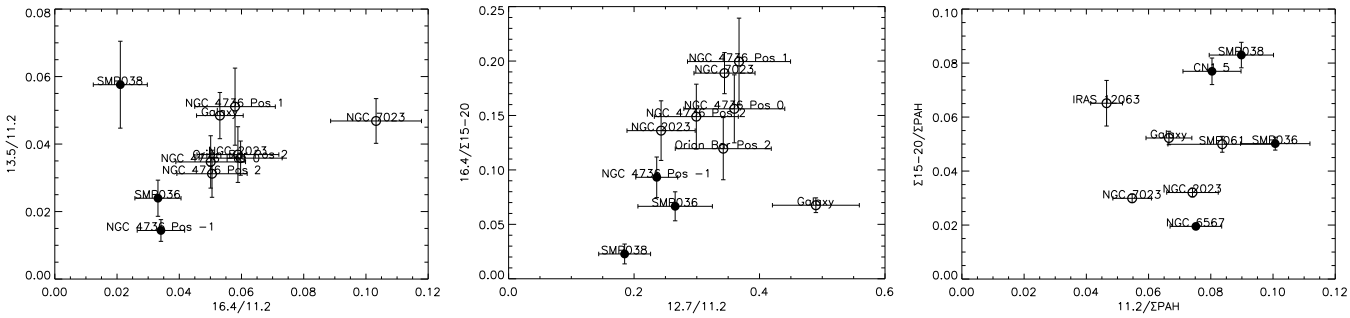

Fig. 7. Three tentative band strength correlations. Peeters et al. (2002) class A sources are shown as open circles and class B sources as filled circles.

($C_{48}H_{20}$) and aenzo[a]fluoranthene ($C_{20}H_{12}$). For six of these molecules the number of experimental and theoretical bands were the same and the assignment was trivial. For the other molecules, if there were more theoretical than experimental bands, there were always two theoretical bands with very similar positions; we assume that these two bands merged into a single band in experiment, and averaged the position of the two theoretical bands. In the cases where there were more experimental bands than theoretical bands, there were always two experimental bands with very similar positions. We assumed that a site splitting of the band had occurred and averaged the position and intensity of the two experimental bands. The best scale factor for the 15−20 μm region was found to be 0.956. This scale factor is very similar to the value of 0.958 for the mid-IR and also very similar to that found for the far-IR (Mulas et al. 2006; Mattioda et al. 2009). Therefore, we adopt a scaling factor of 0.958 for all calculated PAH bands. In Fig. 8, we illustrate the good agreement between the computed and experimentally measured band positions and band strengths by comparing the computed and measured (Hudgins et al. 1994) spectra of neutral naphthalene ($C_{10}H_8$) from 5 to 25 μm (2000 to 400 cm^{-1}).

When comparing astronomical *emission* spectra to computed PAH *absorption* spectra, band shape, natural line width, band shifts inherent to the emission process and relative band intensities must be taken into account. Two schools of thought exist on the origin of the observed band shapes. True isolated harmonic oscillators have *Lorentzian* emission profiles and are considered by one school. Since intermolecular energy transfer is fast compared to emission time scales, the emitting atoms of the PAH molecule find themselves in a constantly changing interaction potential. This leads to anharmonic shifts in peak position, that may well be the origin of the red-shaded, distinctly non-Lorentzian, observed profiles (Barker et al. 1987; Cook & Saykally 1998; Pech et al. 2002). The other school considers *Gaussian* emission profiles. In this approach the astronomical PAH features are believed to be the blending of slightly different relatively narrow Lorentzian profiles. The peak positions of the harmonic oscillators contributing to a feature are then distributed randomly around a mean position. This requires the presence of a large and diverse family of PAH molecules. Support for both schools of thought exist (cf., Tielens 2008). Consistent with both schools, we adopt a Lorentzian profile for each individual PAH transition. We note that, when taking Gaussian profiles in the comparisons hereafter, the differences are non-essential.

Concerning the line width, those observed for the bands between 15−20 μm in astronomical spectra range between 4−8 cm^{-1} (e.g., van Kerckhoven et al. 2000; Moutou et al. 1998). We have adopted an average value of 6 cm^{-1} here. This is substantially narrower than for the mid-IR PAH emission features,

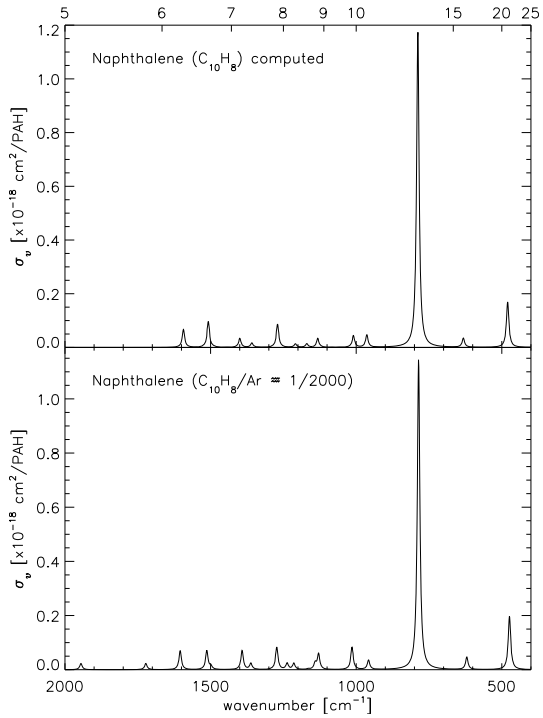

Fig. 8. The synthetic IR absorption spectrum of naphthalene compared to the constructed spectrum from its measured absorption cross-sections in an Argon matrix (Hudgins et al. 1994). The *FWHM* of the Lorentzian absorption profiles are set to 10 cm^{-1}.

where a line width of 10−30 cm^{-1} is more characteristic (see Peeters et al. 2004).

Turning to the band position, since a small (anharmonic) redshift is intrinsic to the emission process, a redshift must be applied to the computed absorption spectra. In the comparisons with astronomical spectra in Sect. 4, the computed spectra are red-shifted by the canonical value of 15 cm^{-1} (≈0.4 μm at these wavelengths). This value is consistent with the shifts measured in a number of experimental studies in the mid-IR (Cherchneff & Barker 1989; Flickinger et al. 1990, 1991; Colangeli et al. 1992; Brenner & Barker 1992; Joblin et al. 1995; Williams & Leone 1995; Cook & Saykally 1998). Recently these effects have been summarised by Bauschlicher et al. (2009). However, the PAH emission process is complicated and not yet fully understood and 15 cm^{-1} may be somewhat overestimated. In reality, the redshift depends on the (non-constant) anharmonicity of the individual mode's contribution to the emission. Therefore, no single "true" value can be given for the redshift and this uncertainty has to be

kept in mind when evaluating the results. Note that this shift is *not* applied to the computed spectra here, in Sect. 3.

Relative emission band intensities depend on the PAH temperature, which changes as the PAH emits, and should be taken into account. Although several, generally more sophisticated, approaches could be conceived, here that of the single PAH, single photon excitation is taken. The thermal approximation is used to determine the emission spectrum and radiative relaxation is taken into account (see also Sect. 4.3; Bakes et al. 2001). Given the current state of our knowledge regarding the molecular physics of the emission process and the very large number of different PAHs involved, a detailed, more sophisticated model is not warranted at this time.

3.2. The influence of structure, composition, charge and size

3.2.1. Structure

Fundamental vibrations associated with the chemical subgroups making up the molecule produce the PAH mid-IR emission, e.g., the 11.2 μm band arising from the solo C−H out-of-plane bending mode in neutral PAHs. Bands in the 15−20 μm region are characteristic for C−C−C bending modes. Hence, while the C−C and C−H stretching and bending modes are characteristic for PAHs as a class, the C−C−C bending modes are expected to be more molecule specific. In planar molecules, such as PAHs, some of these modes resemble "drumhead" vibrations. Just as with percussion instruments, in which the vibrations depend on the size, shape and tautness of the membrane, so too with PAHs. Although the pure radial drumhead modes generally lay far beyond 20 μm (e.g., the corresponding (0, 2) ideal membrane mode for circumcircumcoronene ($C_{96}H_{24}$) lies at 76.5 μm; Mattioda et al. 2009), skeletal components can contribute to the emission between 15−20 μm. We will illustrate this with spectra of a number of well-chosen groups of PAHs with common characteristics. Figure 9 shows the structures of the PAHs considered here and Fig. 10 presents the average 15−20 μm spectra of the species that make up a group. In the average, all spectra have equal weight. For convenience, these spectra have been compared to the continuum subtracted, hi-resolution spectrum of NGC 7023 (position B of Werner et al. 2004b).

We start out with the average spectrum of the large compact shaped PAHs considered by Bauschlicher et al. (2008), labelled *compact* in Fig. 10. The structures are shown in Fig. 9a. Figure 11 shows the 15 to 20 μm spectra of each of these species in their neutral and singly charged forms. The majority of these PAHs have prominent absorption bands that fall within the region of the astronomical emission features. With the exception of the anion spectra of $C_{66}H_{20}$ and $C_{130}H_{28}$, Fig. 11 shows that these spectra, both concerning band strengths and band positions, are largely independent of charge. There is an indication that, within this class of compact PAHs, the strongest band shifts with increasing size towards shorter wavelength and that the spectrum becomes richer.

Next, consider the spectra of the large PAHs with irregular edge structures that make up the average spectrum shown in the panels labelled *irregular* of Fig. 10. Their structures are shown in Fig. 9b. The 15 to 20 μm spectra of each of these species' neutral and singly charged forms are shown in Fig. 12. Compared to the spectra of the compact PAHs, the spectra of the irregular PAHs are richer, with many more bands and much more variation between the spectra from one species to the next. The spectrum of $C_{120}H_{36}$ is somewhat exceptional in that it is dominated by one prominent band that dwarfs all other features. These

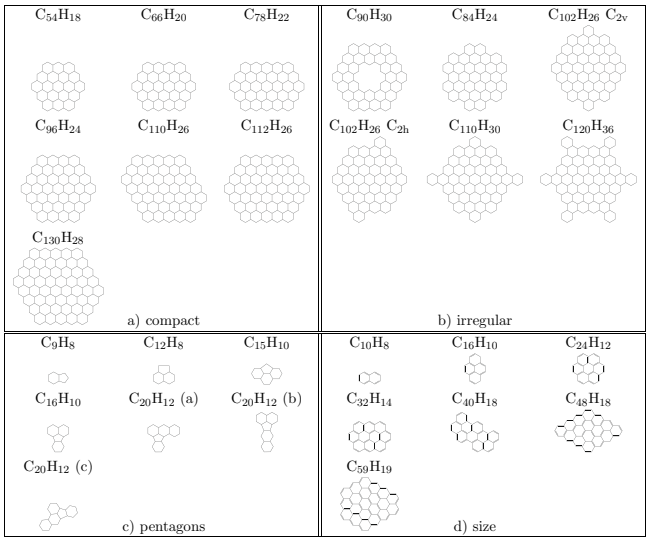

Fig. 9. Overview of the groups of PAHs studied here.

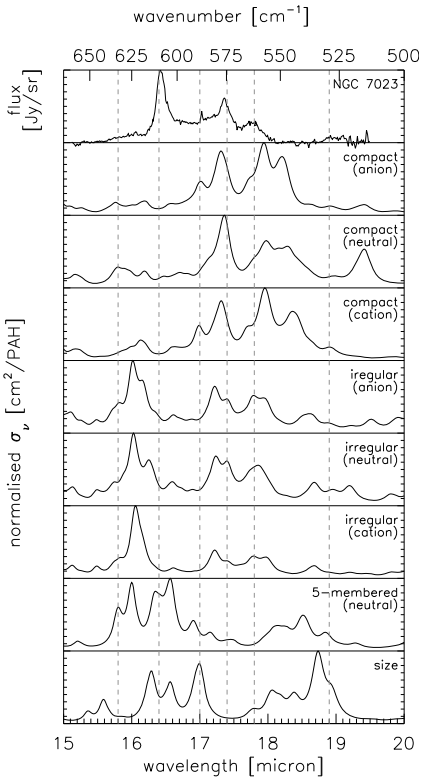

Fig. 10. The hi-resolution continuum subtracted spectrum of NGC 7023 (position B of Werner et al. 2004b) compared to the averaged, computed and normalised to unity spectra of the different groups of PAHs shown in Fig. 9. A *FWHM* of 6 cm^{-1} is taken for the Lorentzian band profiles and a redshift of 15 cm^{-1} is applied.

differences in behaviour between the spectra of the compact PAHs versus the spectra of the similar sized, but irregular PAHs arises for two separate reasons. First, the similarity in molecular structure for the compact PAHs gives rise to very similar C−C−C bending modes and, as the molecule increases in size, slowly more bending modes are present. In contrast, the large variety in molecular edge structure for the irregular PAHs allow many different C−C−C bending modes. Second, when looking at the structure of $C_{120}H_{36}$ in Fig. 9b, it is noted that it is similar

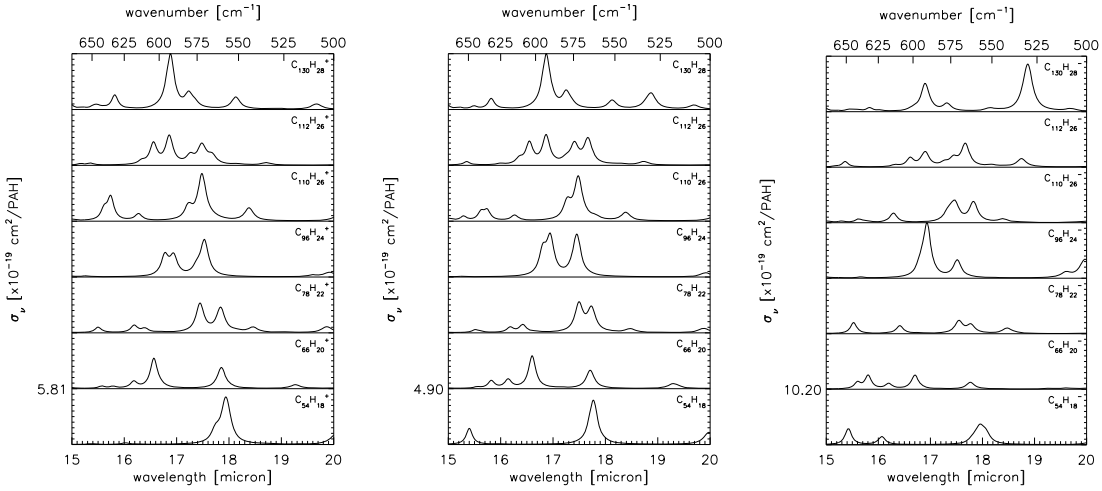

Fig. 11. Computed absorption spectra from 15−20 μm for very large *compact* PAH cations, neutrals and anions. A *FWHM* of 6 cm^{-1} is taken for the Lorentzian band profiles and the bands are *not* red shifted.

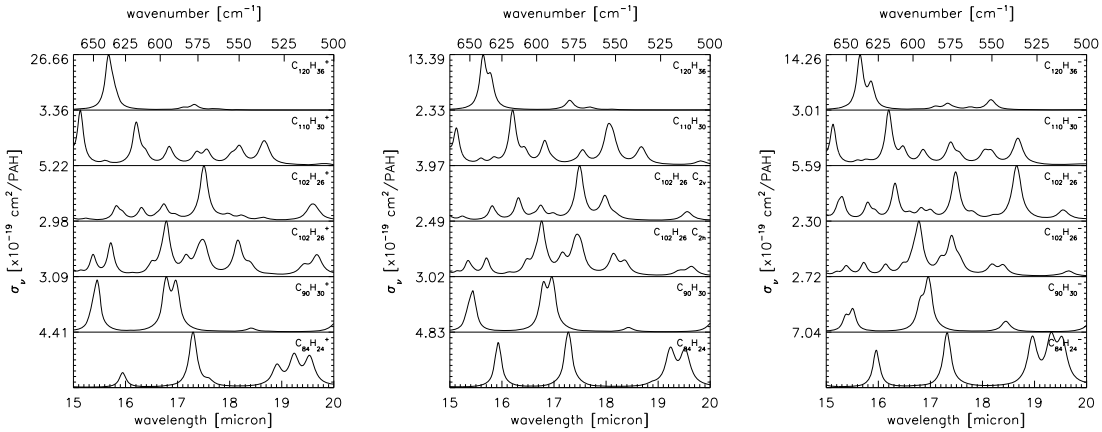

Fig. 12. Synthetic absorption spectra from 15−20 μm for very large *irregular* PAH cations, neutrals and anions. A *FWHM* of 6 cm^{-1} is taken for the Lorentzian band profiles and the bands are *not* red shifted.

to that of $C_{96}H_{24}$ in Fig. 9a, with the difference that the former has six extra pendent hexagonal rings. The strong band near 15.6 μm in the spectrum of $C_{120}H_{36}$ is totally absent in the spectrum of $C_{96}H_{24}$. Analysis of the modes producing the 15.6 μm band reveals that vibrations of the pendent rings are involved. The two modes that produce bands here are the in-sync, out-of-plane motion of the pendent rings as a whole, including the quartet hydrogens, and the in-phase, planar vibration of two opposite carbons of the pendent rings, known as the "breathing-mode" (van Kerckhoven et al. 2000). Figure 13 illustrates these modes. Compared to $C_{110}H_{30}$, a similar large PAH, but with two pendent rings, the in-plane mode is shifted to 15.13 μm and the two out-of-plane modes shift to 14.9 and 16.2 μm, respectively. This suggests that mixing with the central core plays a role in determining the exact location of the pendent ring bands. Unfortunately, due to our limited sample, we cannot investigate this interrelationship in detail.

In connection with pendent rings, Fig. 14 compares the spectra of PAHs containing 5-membered rings and/or pendent *hexagonal* rings. The average 15 to 20 μm spectrum of the PAHs with a 5-membered ring (see Fig. 9c) is shown in Fig. 10. While several of these PAHs have been analysed in earlier studies, the spectra of the three smallest species have not yet been considered. The spectra of the molecules that contain a pendent hexagonal ring all have their strongest band around 16 μm and a shift to shorter wavelengths is apparent when the molecules get larger. Figure 14 confirms earlier statements that it is not the pentagons, but rather the pendent rings that systematically produce a band around 16 μm (van Kerckhoven et al. 2000).

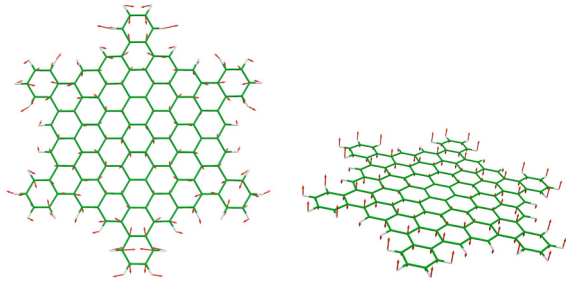

Fig. 13. Graphical illustration of the fundamental vibrations involving the pendent rings in $C_{120}H_{36}$ responsible for the band at 15.6 μm. *Left*: pendent ring "breathing" mode. *Right*: pendent ring "flapping" mode.

3.2.2. Charge

Next, we consider the impact of charge on the 15−20 μm features. The right column in Fig. 15 shows the spectra for 5 different charge states of $C_{96}H_{24}$. This figure illustrates that charge plays very little role in the 15 to 20 μm spectra of this molecule.

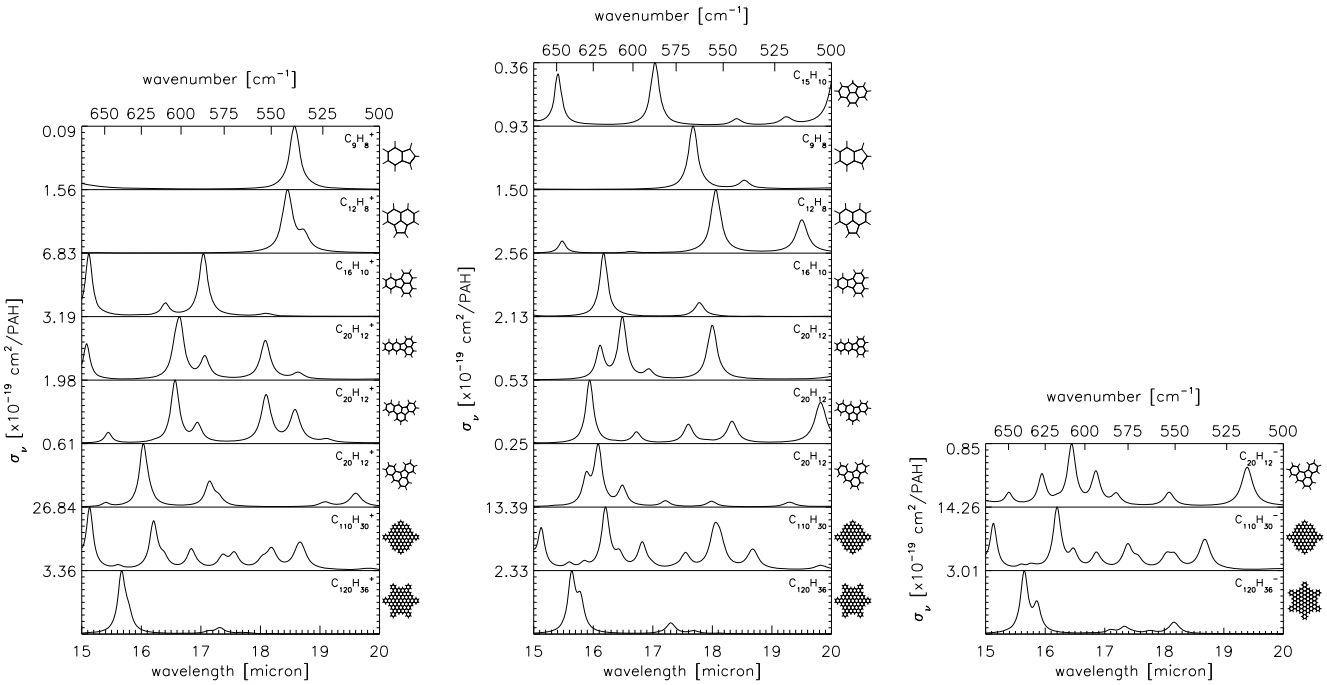

Fig. 14. Synthetic neutral and singly charge absorption spectra from 15−20 μm for PAHs containing 5-membered rings and/or pendent hexagonal rings. Note that for $C_{15}H_{10}$ only the spectrum of the neutral is available. Anion spectra are only available for three species. A *FWHM* of 6 cm^{-1} is taken for the Lorentzian band profiles and the bands are *not* red shifted.

Comparable results were found from a similar study on the smaller PAH, $C_{48}H_{20}$. Interestingly, a weak trend in the relative strength of the bands around 16.9 and 17.5 μm is apparent when going from anions to neutrals to multiply charged states.

3.2.3. Nitrogen incorporation

The substitution of a few nitrogen atoms within the carbon skeleton of large PAH molecules has been found to shift the strong mid-IR band near 6.2 μm (due to C−C modes; Peeters et al. 2002; Hudgins et al. 2005; Bauschlicher et al. 2009). Here, we investigate the influence of nitrogen incorporation on the 15−20 μm spectrum and the possible connection with the mid-IR on the prototypical large PAH $C_{96}H_{24}$. The spectra of the cation form of several $C_{95}H_{24}N$ isomers are shown in the middle column of Fig. 15. The corresponding isomer structures are given in Fig. 16. We note that PAH structures in which the nitrogen is replacing an outer carbon position are not included since these do not match the astronomical 6.2 μm band position (Mattioda et al. 2003; Hudgins et al. 2005). The spectra have been ordered by substitution depth of the exchanged carbon atom. Two bands appear at very much the same position, independent of the nitrogen substitution pattern and are nearly identical to the pure carbon spectrum. The only effect seems to be a subtle variation in the relative strength of these bands but there is no apparent trend with the depth of the substitution.

3.2.4. Size

Lastly, we consider the role of PAH size on the 15−20 μm wavelength region. The left panel in Fig. 15 shows the 15−20 μm spectra as PAH size is increased from 10 to 130 carbon atoms for the *compact* PAHs shown in Figs. 9a, d. Figure 15 shows that all PAHs have spectroscopic structure between 15−20 μm in their spectra. It is interesting that once the PAHs have more than about 30 carbon atoms, they become particularly rich in features.

3.3. "Blind" search

We performed a "blind" database search of the pure PAH species that have their strongest band between 15−20 μm at the two major astronomical PAH band positions of 16.4 or 17.4 μm. This provided several new insights. First, while a dominant band in this wavelength range does require PAHs with sizes exceeding 24 carbon atoms, no clear structural class could be identified whose members all show a band near 17.4 μm[1]. Furthermore, the 15−20 μm region is more crowded with bands when a strong 17.4 μm band is present. Second, the 16.4 μm band tends to be associated with pendent hexagonal rings, consistent with the conclusions by Peeters et al. (2004) and the discussion in Sect. 3.2. In this case the 15−20 μm region generally is clear of other features and the 16.4 μm band clearly dominant. In a few cases, there is a band near 16.4 μm when the 15−20 μm region is also rich in other features, which are of comparable strength. Ricca et al. (2010) note that their PAH spectra typically show a band around the astronomical 17.8 μm position. Although no "blind" search has been performed for this band, Figs. 10−15 also consistently show a feature near the astronomical position.

3.4. Summary

Summarising, all PAHs in the database have bands between 15−20 μm. From all groups of PAHs considered, no systematics appear, except for those PAHs containing pendent rings. PAHs with irregular structure have particularly rich spectra with multiple strong bands in this wavelength range. Small (~50 carbon

[1] After taking the anharmonic redshift into account.

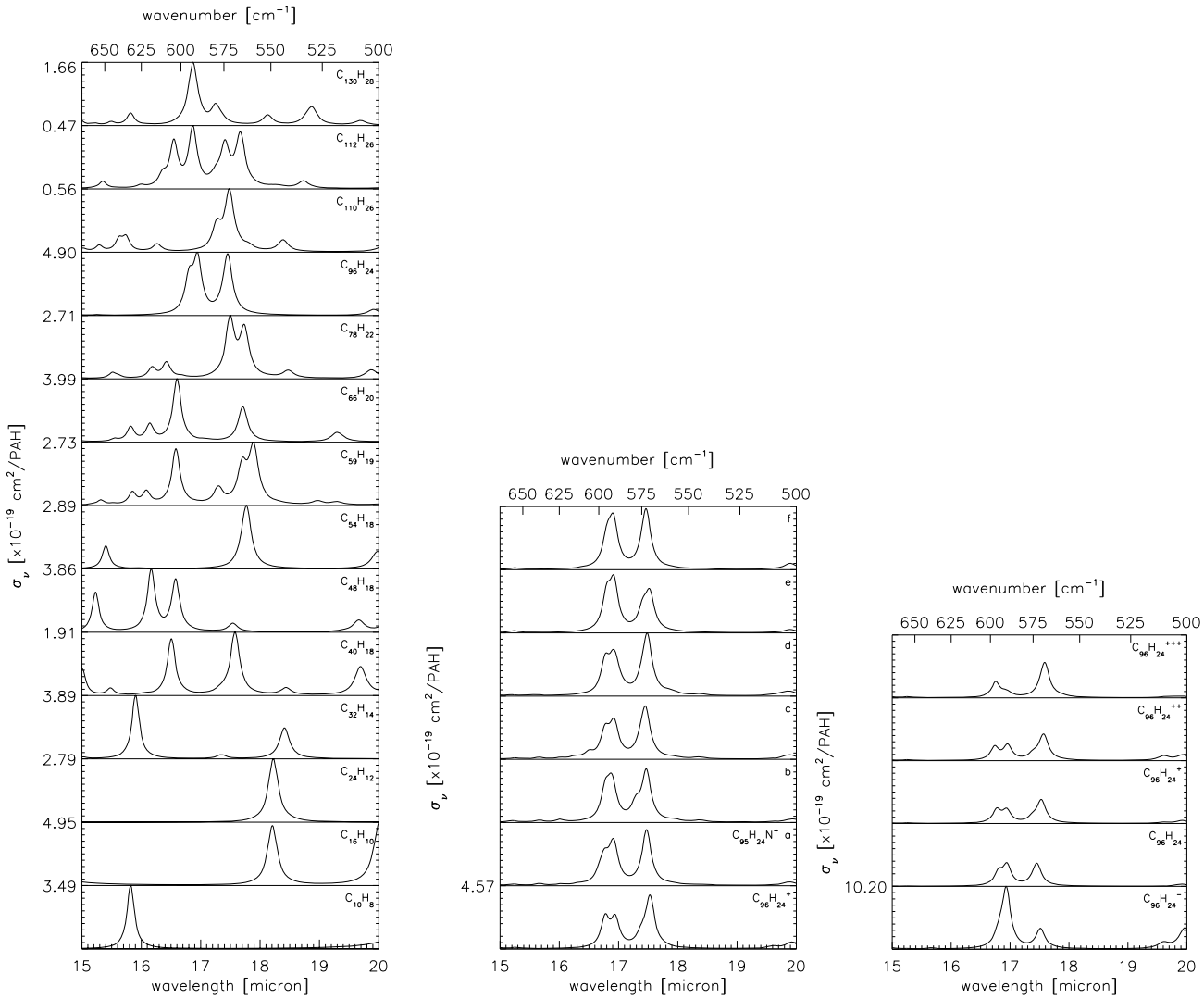

Fig. 15. The influence of the size (*left*), incorporation of nitrogen in the ring (see Fig. 16 for the substitution pattern; *middle*), and charge state (*right*) on the bands between 15−20 μm. A *FWHM* of 6 cm^{-1} is taken for the Lorentzian band profiles.

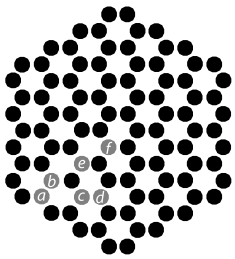

Fig. 16. Single nitrogen substitution pattern for the spectra of $C_{96}H_{24}N$ in *the middle panel* of Fig. 15.

atom) compact PAHs have simpler spectra dominated by a single band but as the size increases their spectra become richer as well. The precise location of this band does depend on the specific molecule under consideration and, apart from a weak dependence on size, there does not seem to be a clear trend. It thus seems, that the 15−20 μm wavelength range probes the specific PAH molecules present in the interstellar PAH family.

However, the database is very incomplete, particularly when considering large species. The database is currently limited to species up to 130 carbon atoms and it is quite possible that the carriers of the bands in the 15−20 μm wavelength region are much larger (Schutte et al. 1993). At this point, we cannot predict whether the same conclusions of this study−bands in the 15−20 μm wavelength region are unique for individual species−holds for very large PAHs as well ($N_C > 200$).

4. Astronomical implications

The astronomical spectra show relatively simple spectroscopic structure between 15−20 μm, with only a few major bands − at 16.4, "17", and 17.4 μm − whose intensity variations demonstrate that they have to be ascribed to independent carriers. Furthermore, there is no relationship between the spectral characteristics of the 15−20 μm C−C−C modes and the 6−9 μm C−C and 11−15 μm C−H out-of-plane modes. An exception is the 16.4 μm band, which shows a connection with the mid-IR C−H and C−C modes, both through strength and feature classification. Furthermore, Sellgren et al. (2007) report the 16.4 μm band in NGC 7023 peaks near the photodissociation front northwest of the irradiating star, as do the 3.3, 6.2 and 11.2 μm features. The relation with the mid-IR PAH is thus well established. The analysis of the synthetic spectra of the PAHs in the NASA Ames PAH IR spectroscopic database reveals that the 15−20 μm wavelength

range is characteristic for individual PAHs and that there is little systematic dependence on PAH class or molecular structure. The absence of a relationship between the C−C−C modes with the C−C and C−H modes in the astronomical spectra is perhaps then not that surprising. While the C−C molecules are very sensitive to class characteristics, the C−C−C modes are not. By the same token, the database reveals that the strength of the C−C and C−H modes are very sensitive to ionisation of the PAH, while the C−C−C modes are not. The only exceptions are that large compact PAHs tend to have most activity close to the astronomical features as do PAHs containing pendent rings. As a rule, PAHs containing pendent rings show a strong band near the astronomical 16.4 μm band (Moutou et al. 2000; van Kerckhoven et al. 2000; Peeters et al. 2004). Overall, the data suggests that−in general – the emission between 15−20 μm is dominated by a few, relatively large (50−200 carbon atom) PAHs that are individually responsible for the recognisable bands in this wavelength region. We note that some sources (e.g., Orion Bar Pos 1) show a broad emission feature in the 15−20 μm region without discernible structure. Such regions may be characterised by a far richer, interstellar PAH family.

4.1. PAH Di-cations

The 18.9 μm band intensity has been reported to increase when moving closer to the irradiating source (NGC 7023; Sellgren et al. 2007). The idea for an increasing degree of ionisation is tempting. However, our analysis shows that the spectra in the 15−20 μm region do not show a strong dependence on charge. Hence, from the point of view of the database, there is no obvious connection to PAH di-cations. In line with our earlier discussion, we suggest that the 18.9 μm band is carried by one specific PAH species which is very stable and hence can survive the harsh conditions close to the exciting star, where it becomes the dominant PAH species. Indeed, Sellgren et al. (2007) suggested the extremely stable fullerene (C_{60}) as a potential carrier. Interestingly enough, the charge effect on the spectrum of $C_{96}H_{24}$, Fig. 15, shows the band strength ratio of the two dominant components increases with increasing degree of ionisation. Therefore, charge might play a role for the "17" μm feature.

4.2. Pendent rings

The interstellar 16.4 μm band might be carried by PAHs containing pendent rings. Support is found through the weak correlation between the strength of the 16.4 and 12.7 μm bands relative to that of the 11.2 μm band (Fig. 7). The observed 12.7/11.2 μm integrated band strength ratio probes the molecular edge structure of the PAHs with a high ratio characteristic for a broken up structure with many corners, such as pendent rings (Hony et al. 2001; Bauschlicher et al. 2009). Similarly, a pendent ring origin of the 16.4 μm band is consistent with the observed weak correlation of the interstellar 16.4 and 13.5 μm bands (Fig. 7), where the 13.5 μm band is due to quartet hydrogens on pendent rings (e.g., the 4 adjacent carbon atoms that have a hydrogen bond). We investigate the latter correlation in more detail. In Fig. 17 the distribution for the 16.4/13.5 μm PAH band strength ratio is shown for the database, where we have added the bands between 16.0−16.6 and 13.4−14.0 μm in the computed spectra and ratioed these. The computed spectra have prior to this been red shifted by 10 cm^{-1} and 15 cm^{-1} for the 10−15 and 15−20 μm regions, respectively (see Bauschlicher et al. 2009). Only pure PAHs containing quartet hydrogens were considered, totalling

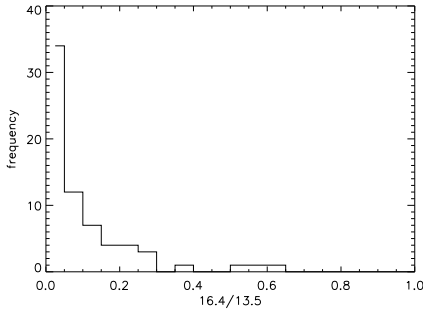

Fig. 17. Distribution of the 16.4/13.5 integrated band strength ratio for the pure, quartet hydrogen containing PAH species in the NASA Ames PAH IR spectroscopic database.

101 spectra. Of these, 27 did not have emission around the astronomical 16.4 μm PAH band position. The absence likely reflects mode coupling with the carbon skeleton, shifting it away from the astronomical 16.4 μm position. The resulting distribution predicts that the intensity of the astronomical 16.4 μm band is between 2 and 20% of that in the astronomical 13.5 μm band. This is very difficult to reconcile with the observed strength ratio of these two bands in the interstellar spectra (∼1.5; Fig. 7). Perhaps, dehydrogenation may be a (preferential) characteristic of pendent rings, enhancing the observed 16.4 to the 13.5 μm band strength ratio. We also note that, generally the out-of-plane bending mode occurs at a characteristic wavelength of 13.5 μm (Hony et al. 2001). However, in some pendent rings the out-of-plane C−H bending mode combines with the C−C−C modes, producing one strong band near 15.6 μm (cf., Fig. 13), further enhancing this ratio. Finally, Ricca et al. (2010) show, that as a class, structures with "pointy" edges (e.g., rhombus shaped species) also produce a band near the astronomical 16.4 μm feature. This type of structure does not posses quartet hydrogens.

4.3. PAH temperature

PAH temperature is relevant for the relative band intensities. Figure 18 compares the low-resolution Spitzer IRS spectrum of NGC 7023 (panel a) with the average absorption spectrum of a collection of 7 very large PAHs (panel b; Bauschlicher et al. 2008). Also shown in this figure is the emission spectrum, including the temperature cascade, from the mixture after each PAH absorbed a 4 eV photon (panel c). The emission spectrum has been computed considering conservation of energy:

$$4\pi \sum_i \sigma_i \int_{T_i}^{T_{\max}} B(\nu_i, T) \left[\frac{\mathrm{d}T}{\mathrm{d}t}\right]^{-1} \mathrm{d}T = hc\nu_{\mathrm{uv}}.$$

Here σ_i [cm^2] is the absorption cross-section in mode i; $B(\nu_i, T)$ [erg s^{-1} cm^{-2} Hz^{-1} sr^{-1}] is Planck's function at frequency ν [cm^{-1}] in mode i and temperature T [Kelvin]; $\mathrm{d}T/\mathrm{d}t$ [Kelvin s^{-1}] is the cooling-rate and ν_{uv} [cm^{-1}] is the frequency of the absorbed ultraviolet/visible photon. The sum is taken over all modes and the integral runs from the initial PAH temperature (T_i) up to the maximum attained temperature ($T_{\max}$ [Kelvin]) by the PAH molecule upon absorption of the photon. The cooling-rate and the maximum attained temperature are determined through the heat capacity, for which the description for isolated harmonic oscillators is used. Figure 18 demonstrates that the average theoretical absorption spectrum reproduces the band positions of the overall astronomical spectrum well and, in the spectrum including the temperature cascade,

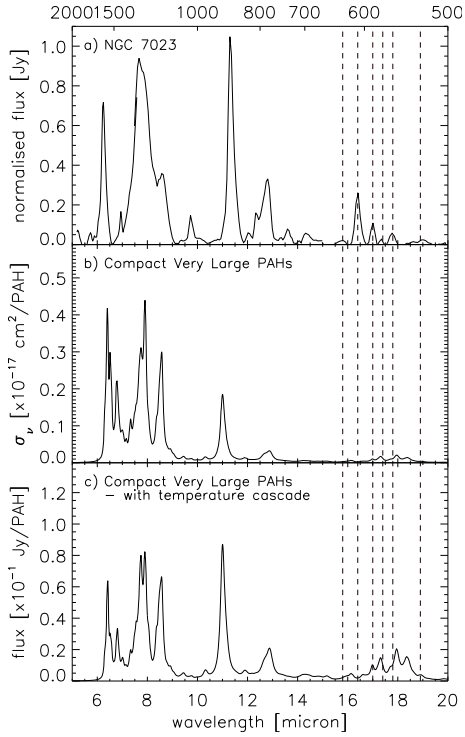

Fig. 18. The 5−20 μm low-resolution spectrum of the reflection nebula NGC 7023 (*top panel*) compared to the average *absorption* spectrum of 7 singly positive ionised very large PAHs ($C_{54}H_{18}$ to $C_{130}H_{28}$; panel **b)** and the computed *emission* spectrum of the PAH mixture including the temperature cascade. The structures of these PAHs are shown in Fig. 9a. A *FWHM* of 15 and 6 cm^{-1} has been used for the Lorentzian emission profiles between 5−15 and 15−20 μm respectively. The spectrum of NGC 7023 has been baseline corrected and PAH plateaus have been removed as described in Sect. 2.2. A redshift of 15 cm^{-1} has been applied to the synthetic data to facilitate comparison with the astronomical spectrum.

how the intensity of the 15−20 μm band increases significantly with respect to the intensity of the shorter wavelength features. Given the nature of the excitation-emission process, band positions and relative intensities of prominent bands in *neighbouring* wavelength regions must also be consistent with the astronomical emission spectrum, and vice-versa. Indeed, the computed emission spectrum including the temperature cascade shows the right number of bands at about the right relative strength in the 11−15 and 15−20 μm wavelength regions. Close agreement with the astronomical bands between 5 and 10 μm is less important since these may originate in smaller PAHs than do the longer wavelength features (e.g., Bauschlicher et al. 2009; Schutte et al. 1993). The computed spectra do not match the observed spectra well in detail. That may partly reflect the inherent uncertainties and limitations in the computational methods and the anharmonicity of the emission process. In addition, experimental and computational studies may not yet have zoomed in on the "right" family of interstellar PAHs.

4.4. PAH size

Since PAH temperature and size are linked through the heat capacity, larger PAHs attain a lower temperature than their smaller counterparts upon the absorption of the same amount of energy. This implies that the smallest PAHs do not contribute much to the emission in the 15−20 μm region (Schutte et al. 1990; Bauschlicher et al. 2009). Conversely, we can estimate an average size of the PAHs from the observed spectra. Theoretically, the emission ratios are given by,

$$I_{\sum 15-20}\Big/I_{\sum 6-9} \simeq (\sigma_{\sum 15-20}\Big/\sigma_{\sum 6-9}) \times \hat{I}_{\nu,\sum 15-20}(T_{\max})\Big/\hat{I}_{\nu,\sum 6-9}(T_{\max})$$

and similarly for $I_{\sum 15-20}/I_{\sum 10-15}$. Here, the intrinsic cross-section ratios ($\sigma_{\Sigma 15-20}/\sigma_{\Sigma 6-9}$ and $\sigma_{\Sigma 15-20}/\sigma_{\Sigma 10-15}$) are determined from the database, similar to what was done for the 16.4/13.5 μm band strength ratios in Fig. 17. $\hat{I}_\nu$ is the band intensity including the temperature cascade, which depends on the maximum attained temperature ($T_{\max}$). Both can be found using the formalism described in Sect. 4.3. The results of this exercise are shown in Fig. 19. Only PAHs with more than 20 carbon atoms have been considered for the histograms and the plateau emission between 15−20 μm has been included for the C−C−C band strength of the astronomical sources. Because the C−C−C/C−C ratio spans a wider wavelength range than the C−C−C/C−H ratio, the former is a more sensitive probe of the size of the emitting, interstellar PAHs. The comparison to the C−C modes indicates a size of $\sim 10^3$ carbon atoms, while the C−H comparison spans a somewhat broader range of 10^2−10^3 carbon atoms. This difference in inferred size may reflect the (unknown) admixture of neutral (C−H carriers) and cationic (C−C carriers) PAHs contributing to the 15−20 μm range.

These sizes inferred for the C−C−C carriers are much larger than derived from the ratio of the 3.3 μm C−H stretching mode to the 11.2 μm C−H out-of-plane bending mode of 50−100 carbon atoms. Furthermore, comparing the spectra in Fig. 18 suggests a characteristic size of $\sim 10^2$ carbon atoms when only the narrow emission features between 15−20 μm are considered. Thus, besides extremely large PAHs dominating the 15−20 μm (plateau) emission with a few large PAHs producing the narrow features, there should also be (some) smaller PAHs which dominate the 3.3 and 11.2 μm C−H modes but do not contribute greatly to longer wavelength emission. Now, we consider it unlikely that such large PAHs ($N_C > 200$) consist of single sheets of aromatic molecules, but rather that these are clusters of smaller PAHs. Such clusters are likely to incorporate impurities, which will influence the fundamental PAH frequencies in the 15−20 μm region. Even so, it is unlikely that sole large PAHs dominate the size range, whether they are single free floating species or clusters of smaller PAHs. From that perspective, it is unclear why the 15−20 μm range is dominated by a few well defined bands or equivalently, why large PAHs or PAH clusters as a class would be characterised by common vibrational frequencies in the 15−20 μm wavelength range. We emphasise that there is no indication for this behaviour in the (smaller) PAHs contained in the NASA Ames IR spectroscopic database. Of course, there is always the possibility that we missed a class of species or the "right" species is not contained in the database.

4.5. PAH 15–20 μm plateau

Currently there is a debate in the literature on the origin of the plateaus beneath the strong PAH bands. In one view, the plateaus arise from the blending of numerous Lorentzian band shapes, common to most PAH and PAH-related molecules. Another view is that the plateaus are produced by overlapping bands from a distinct family of PAH species, PAH clusters and VSG, which might or might not, spatially co-exist with the carriers of the stronger features. In this work the broad "17" μm feature is

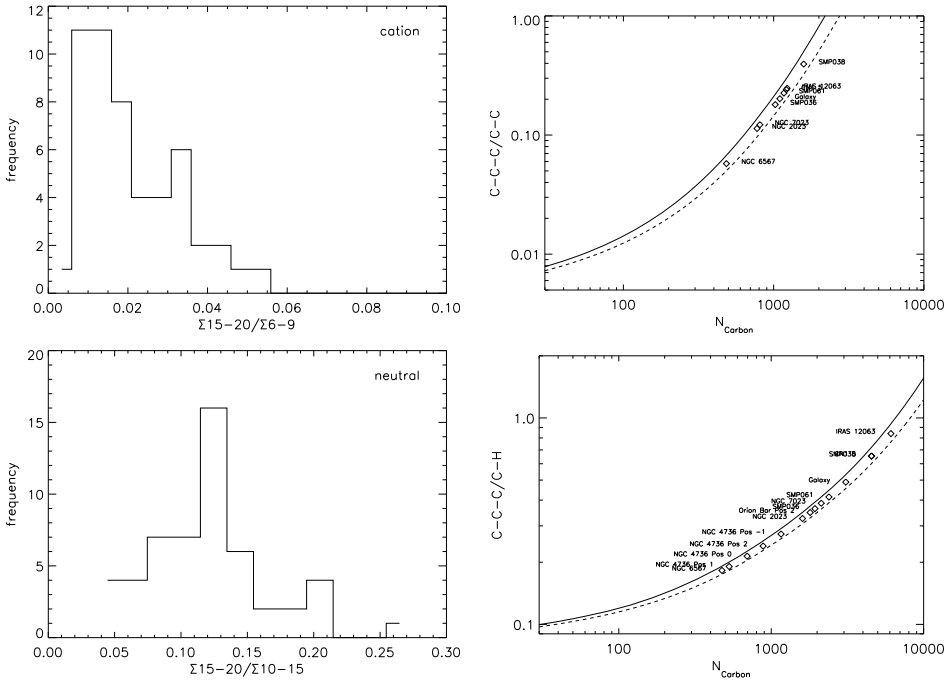

Fig. 19. Estimated sizes for the PAH emitters dominating the total emission between 15−20 μm (C−C−C modes) and the major contributors to the emission between 6−9 μm (C−C modes) from an intrinsic value for the cross-section ratio of 0.013, taken from the presented distributions, where only PAHs with more than 20 carbon atoms were considered. Similarly, by using the 10−15 μm (C−H modes) integrated PAH band strength with an intrinsic value for the cross section ratio of 0.13. The thick solid line is at an average photon energy of 8 eV and the dashed line at 10 eV. The observed ratios for these modes for each source are indicated by diamonds.

treated as a plateau and the size analysis presented above, suggests indeed a different carrier for the plateau than for the narrow features. An analysis similar to that of Rapacioli et al. (2006), should shed light on the characteristics of the clusters. However, NGC 6567 shows a unique "17" μm feature, which does not resemble the plateau-only sources, but is more similar to the Gaussian features used by Sellgren et al. (2007) and Smith et al. (2007b). NGC 6567 might well prove to be key in understanding the exact nature of the "17" μm band.

4.6. Individual PAHs

Lastly, consider the computed spectra of a few individual large compact PAHs. Astronomically, the group of large compact PAHs is particularly relevant because of their high stability owing to their super aromaticity and size. Within this class, PAHs that produce bands which coincide with some of the astronomical bands between 15−20 μm, while not showing activity outside the astronomical emission complex or inconsistent intensity ratios, are $C_{130}H_{28}$ and $C_{110}H_{26}$ (see Fig. 11). Figure 20 compares the 5−20 μm spectrum of these species in several charge states with the low-resolution astronomical spectrum of NGC 7023. This comparison shows that the single cation of $C_{130}H_{28}$ has a feature that redshifts to about 17.4 μm, in good agreement with the (weak) astronomical band position. While the peak position match is not as good for $C_{110}H_{26}$, the clear feature near 18 μm in the spectra of the cation and neutral forms of this PAH lies close to the 17.9 μm astronomical sub-peak. Of course, one coincidence does not constitute an identification and it will be very important to test these suggestive species by searching for their lowest fundamental radial drumhead mode in the far-IR using Herschel or SOFIA.

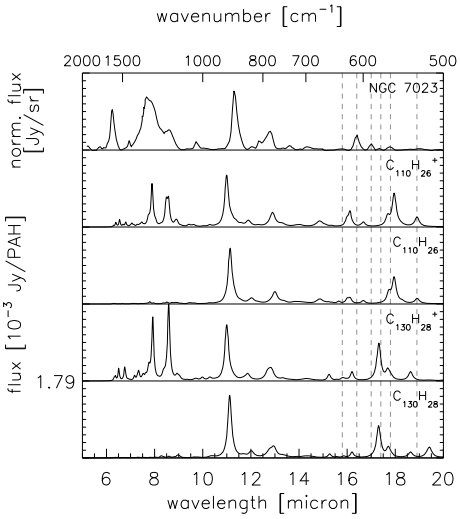

Fig. 20. The PAH features between 5−20 μm in the low-resolution spectrum of NGC 7023 (position B of Sellgren et al. 2007) compared with the emission spectra of neutral and single positively ionised $C_{110}H_{28}$ and $C_{130}H_{28}$. The spectrum of NGC 7023 has been baseline corrected and pedestals have been removed as described in Sect. 2.2. The emission spectra of $C_{110}H_{26}$ and $C_{110}H_{26}$ are at an excitation temperature of 200 K to enhance the features between 15−20 μm. The computed spectra have been red-shifted by 15 cm^{-1} to account for the shift inherent for the emission process. The spectrum of NGC 7023 is reproduced from Sellgren et al. (2007). A *FWHM* of 15 and 6 cm^{-1} is used for the emission profiles between 5−15 and 15−20 μm respectively. See text and Bauschlicher et al. (2009) for discussion of the redshift.

5. Summary and conclusions

The astronomical spectra show six distinct components at 15.8, 16.4, "17", 17.4, 17.8 and 18.9 μm. *These bands do not*

correlate with each other, implying these bands must be carried by independent molecular species or classes of species. Except for the 16.4 μm band, no connection with any of the mid-IR bands was found, both in band strength or feature classification. This implies the 15−20 μm bands are not sensitive to the same (molecular) parameters as the mid-IR features. For specific objects, NGC 6567 shows a unique 15−20 μm spectrum, only consisting of the broad "17" μm band and this object may well be key in understanding the nature of this specific feature.

Using synthetic spectra, we studied the emission characteristics between 15−20 μm for different groups of PAHs (structure, charge, composition and size). Within most of these groups no systematic behaviour is found. However, the 15−20 μm region is clearly the transition region from features corresponding to full skeleton (C−C−C) modes to the mid-IR bands, which arise from chemical subgroup and individual bond stretching and bending modes. The data suggest that−in general−the emission between 15−20 μm is dominated by a very limited number of relatively large (50−200 carbon atom) PAHs that are individually responsible for the recognisable narrow bands in this wavelength region. The group of PAHs containing pendent rings is attractive to explain the astronomical 16.4 μm feature. However, this requires a strength of the 13.5 μm which does not agree with observations.

Overall, we want to emphasise that analysis of the 15−20 μm wavelength range impresses a relatively simple view of the interstellar PAH family, where a few, specific, large PAHs dominate the emission characteristics when the region shows distinct features, e.g., NGC 7023. Those sources with a broad emission plateau between 15−20 μm would then have a much more diverse family, e.g., IRAS 12063-6259. It should be stressed though, that PAHs with up to only 130 atoms are included in the database and it is very biased towards smaller sizes. Furthermore, this study focused mainly on the pure PAHs that dominate the database. PAH-related species such as PAH clusters, which often incorporate impurities, are also not included. Therefore, some of the key molecules responsible for the emission in this region are likely under represented. The incompleteness with respect to large PAHs in the database, further implies the situation for Herschel, SOFIA and ALMA with forthcoming far-IR and radio data, is dire. Further insight can be acquired by calculating the spectra of larger molecules. The pioneering observations of long wavelength features are essential to extend our understanding of the astronomical PAH population, the identification of possible individual PAHs that dominate the emission and the diverse roles of PAHs in astrophysics. Additionally, these long wavelength observations will open up a new regime in low energy astrophysics. Finally, in the post-Spitzer era, a complete set of objects should be investigated to re-establish the results obtained by the previous mid-IR missions and chart the road map for the new missions.

Acknowledgements. C.B. thanks Kris Sellgren for her help and willingness to share their data. L.J.A. gratefully acknowledges sustained support from NASA's Laboratory Astrophysics and Astrobiology programs. Alessandra Ricca thanks the NASA Astronomy and Physics Research and Analysis, the NASA Astrophysics Data Analysis and the NASA Astrophysics Theory and Fundamental Physics programs for their generous financial support.

References

Bakes, E. L. O., Tielens, A. G. G. M., & Bauschlicher, Jr., C. W. 2001, ApJ, 556, 501
Barker, J. R., Allamandola, L. J., & Tielens, A. G. G. M. 1987, ApJ, 315, L61
Bauschlicher, Jr., C. W., Peeters, E., & Allamandola, L. J. 2008, ApJ, 678, 316
Bauschlicher, Jr., C. W., Peeters, E., & Allamandola, L. J. 2009, ApJ, 697, 311
Becke, A. D. 1993, J. Chem. Phys., 98, 5648
Bernard-Salas, J., Peeters, E., Sloan, G. C., et al. 2009, ApJ, 699, 1541
Boersma, C., Bouwman, J., Lahuis, F., et al. 2008, A&A, 484, 241
Boulanger, F., Boisssel, P., Cesarsky, D., & Ryter, C. 1998, A&A, 339, 194
Brenner, J., & Barker, J. R. 1992, ApJ Lett, 388, L39
Cahn, J. H., Kaler, J. B., & Stanghellini, L. 1992, A&AS, 94, 399
Caswell, J. L., & Haynes, R. F. 1987, A&A, 171, 261
Cherchneff, I., & Barker, J. R. 1989, in Interstellar Dust, ed. L. J. Allamandola, & A. G. G. M. Tielens, IAU Symp., 135, 151
Colangeli, L., Mennella, V., & Bussoletti, E. 1992, ApJ, 385, 577
Cook, D. J., & Saykally, R. J. 1998, ApJ, 493, 793
de Zeeuw, P. T., Hoogerwerf, R., de Bruijne, J. H. J., Brown, A. G. A., & Blaauw, A. 1999, AJ, 117, 354
Flickinger, G. C., Wdowiak, T. J., & Boyd, D. A. 1990, in Dusty Objects in the Universe, ed. E. Bussoletti, & A. A. Vittone, Ap&SS Library, 165, 77
Flickinger, G. C., Wdowiak, T. J., & Gomez, P. L. 1991, ApJ, 380, L43
Frisch, M. J., Pople, J. A., & Binkley, J. S. 1984, J. Chem. Phys., 80, 3265
Frisch, M. J., Trucks, G. W., Schlegel, H. B., et al. 2004, Gaussian 03, Revision C.02, Gaussian, Inc., Wallingford, CT, 2004
Galliano, F., Madden, S. C., Tielens, A. G. G. M., Peeters, E., & Jones, A. P. 2008, ApJ, 679, 310
Hony, S., van Kerckhoven, C., Peeters, E., et al. 2001, A&A, 370, 1030
Houck, J. R., Roellig, T. L., van Cleve, J., et al. 2004, ApJS, 154, 18
Hudgins, D. L., & Sandford, S. A. 1998a, J. Phys. Chem. A, 102, 329
Hudgins, D. L., & Sandford, S. A. 1998b, J. Phys. Chem. A, 102, 344
Hudgins, D. L., & Sandford, S. A. 1998c, J. Phys. Chem. A, 102, 353
Hudgins, D. L., Sandford, S. A., & Allamandola, L. J. 1994, J. Phys. Chem., 98, 4243
Hudgins, D. M., Bauschlicher, Jr., C. W., & Allamandola, L. J. 2005, ApJ, 632, 316
Joblin, C., Boissel, P., Leger, A., D'Hendecourt, L., & Defourneau, D. 1995, A&A, 299, 835
Kennicutt, Jr., R. C., Armus, L., Bendo, G., et al. 2003, PASP, 115, 928
Kessler, M. F., Steinz, J. A., Anderegg, M. E., et al. 1996, A&A, 315, L27
Kovács, G. 2000, A&A, 363, L1
Levato, H., & Abt, H. A. 1976, PASP, 88, 712
Mattioda, A. L., Hudgins, D. M., Bauschlicher, Jr., C. W., Rosi, M., & Allamandola, L. J. 2003, J. Phys. Chem. A, 107, 1486
Mattioda, A. L., Ricca, A., Tucker, J., Bauschlicher, Jr., C. W., & Allamandola, L. J. 2009, ApJ, 137, 4054
Moutou, C., Leger, A., & D'Hendecourt, L. 1996, A&A, 310, 297
Moutou, C., Sellgren, K., Leger, A., et al. 1998, in Star Formation with the Infrared Space Observatory, ed. J. Yun, & L. Liseau, ASP Conf. Ser., 132, 47
Moutou, C., Verstraete, L., Léger, A., Sellgren, K., & Schmidt, W. 2000, A&A, 354, L17
Mulas, G., Malloci, G., Joblin, C., & Toublanc, D. 2006, A&A, 460, 93
Pech, C., Joblin, C., & Boissel, P. 2002, A&A, 388, 639
Peeters, E., Hony, S., van Kerckhoven, C., et al. 2002, A&A, 390, 1089
Peeters, E., Mattioda, A. L., Hudgins, D. M., & Allamandola, L. J. 2004, ApJ, 617, L65
Peeters, E., Mattioda, A. L., Kemper, F., Hudgins, D. M., & Allamandola, L. J. 2006, in ed. L. Armus, & W. T. Reach, ASP Conf. Ser., 357, 95
Perryman, M. A. C., Lindegren, L., Kovalevsky, J., et al. 1997, A&A, 323, L49
Rapacioli, M., Calvo, F., Joblin, C., et al. 2006, A&A, 460, 519
Ricca, A., Bauschlicher, Jr., C. W., Mattioda, A. L., et al. 2010, ApJ, 709, 42
Schutte, W. A., Tielens, A. G. G. M., & Allamandola, L. J. 1993, ApJ, 415, 397
Schutte, W. A., Tielens, A. G. G. M., Allamandola, L. J., Wooden, D. H., & Cohen, M. 1990, ApJ, 360, 577
Sellgren, K., Uchida, K. I., & Werner, M. W. 2007, ApJ, 659, 1338
Sloan, G. C., Keller, L. D., Forrest, W. J., et al. 2005, ApJ, 632, 956
Smith, J. D. T., Armus, L., Dale, D. A., et al. 2007a, PASP, 119, 1133
Smith, J. D. T., Draine, B. T., Dale, D. A., et al. 2007b, ApJ, 656, 770
Stanghellini, L., & Pasquali, A. 1995, ApJ, 452, 286
Stephens, P. J., Devlin, F. J., Chabalowski, C. F., & Frisch, M. J. 1994, J. Phys. Chem., 98, 11623
Tielens, A. G. G. M. 2008, ARA&A, 45, 289
Tielens, A. G. G. M., Hony, S., van Kerckhoven, C., & Peeters, E. 1999, in The Universe as Seen by ISO, ed. P. Cox, & M. Kessler, ESA SP-427, 579
van den Ancker, M. E., The, P. S., Tjin A Djie, H. R. E., et al. 1997, A&A, 324, L33
van Diedenhoven, B., Peeters, E., van Kerckhoven, C., et al. 2004, ApJ, 611, 928
van Kerckhoven, C., Hony, S., Peeters, E., et al. 2000, A&A, 357, 1013
Waters, L. B. F. M., Cami, J., de Jong, T., et al. 1998, Nature, 391, 868
Werner, M. W., Roellig, T. L., Low, F. J., et al. 2004a, ApJS, 154, 1
Werner, M. W., Uchida, K. I., Sellgren, K., et al. 2004b, ApJS, 154, 309
Williams, R. M., & Leone, S. R. 1995, ApJ, 443, 675
Zhang, K., Guo, B., Colarusso, P., & Bernath, P. F. 1996, Science, 274, 582